Comparative Study of Stranded and Bar Windings in an Induction Motor for Automotive Propulsion Applications

COMPARATIVE STUDY OF STRANDED AND BAR WINDINGS IN AN INDUCTION MOTOR FOR AUTOMOTIVE PROPULSION APPLICATIONS

BY

HANNAH KOKE, B.Sc.

A THESIS

SUBMITTED TO THE DEPARTMENT OF MECHANICAL ENGINEERING

AND THE SCHOOL OF GRADUATE STUDIES

OF MCMASTER UNIVERSITY

IN PARTIAL FULFILMENT OF THE REQUIREMENTS

FOR THE DEGREE OF

MASTER OF APPLIED SCIENCE

Master of Applied Science (2017) McMaster University

(Mechanical Engineering) Hamilton, Ontario, Canada

TITLE:	Comparative Study of Stranded and Bar Windings in an Induction Motor for Automotive Propulsion Applications
AUTHOR:	Hannah Koke B.A.Sc., (Mathematics and Engineering) Queen's University, Kingston, Canada
SUPERVISOR:	Dr. Ali Emadi
NUMBER OF PAGES:	xv, 102

For Bridget and Carly

Abstract

The source-to-wheel efficiency of today's electrified vehicles already far surpasses the efficiency of strictly gasoline vehicles. As sources of electricity become cleaner and more efficient, and as gasoline becomes more scarce, the need for transporation electrification is increasingly economically and environmentally driven. The automotive industry primarily makes use of permanent magnet synchronous machines (PMSMs) and induction machines (IMs), the latter has the cost advantage of containing no rare earth metals. This thesis studies two different induction motors for electrified powertrain applications using a novel optimization algorithm to create efficiency maps and compare the efficiencies of the two motors. Induction motors are difficult to banchmark due to their complicated control schemes. Each point in their operating range can be achieved with an infinite number of current/slip combinations and therefore has infinite potential efficiencies. The proposed algorithm limits the number of simulations needed to benchmark an induction machine, and provides a clear and unbiased way to compare machines based on losses at their most efficient current/slip combinations over their entire operating range. The proposed algorithm is able to calculate losses within 5% accuracy of simulation values for both machines. The first motor studied makes use of stranded windings and geometry parameters from the Tesla Motors patents. The efficiency map created has a peak efficiency of 96% and

corresponds closely to an efficiency map for a similar motor found in literature. The second motor makes use of copper bar windings, which are easier to manufacture and have lower material costs. Bar windings, typically have lower resistance and stator copper losses at low speeds, but higher effective resistance and stator losses at high speeds due to eddy effects. The motor modelled was intended simply to compare the stranded and bar windings, and to see the advantages and disadvantages. For this reason, no other changes are made to the winding layout or motor geometry, including changes that would reduce the eddy effect. The resultant efficiency map has a peak efficiency of only 90%, performing worse than the stranded wound motor across most of its operating range. At very low speeds, under 1000 rpm, the efficiency of the bar wound machine is better than that of the stranded machine. The bar wound machine also has the advantage of being over 80% efficient everywhere. The author suggests that future research focus on applying the proposed benchmarking algorithm to stator bar motors designed to limit eddy effects. Strategies include changing the slot opening shape, increasing the number of stator bars, and moving the stator bars away from the air gap.

Acknowledgements

This research was undertaken, in part, thanks to funding from the Canada Excellence Research Chairs Program and the Natural Sciences and Engineering Research Council of Canada Discovery Grants Program.

Thank you to my supervisor Dr. Ali Emadi for granting me the opportunity to pursue this research, for his expertise, his time, and for ensuring that my research was interesting, insightful and progressive. I must thank Dr. Emadi also for his compassion and understanding over the last two years. It was an honour to work with Dr. Emadi.

To Dr. Yinye Yang, who had a vital role in supervising my work, thank you for asking me tough questions and ensuring that all results were rigorous and verifiable.

I am grateful to my colleagues in the Canada Excellence Research Chair. Special thanks go to Sandra Castano, Trevor Hadden, Michael Kasprzak, and Rong Yang for their support as we worked alongside one another on the electric motor team. Thank you to Jeremy Lempert and Michael Kasprzak for reading my thesis and providing their feedback.

Thank you to James Jiang for his friendship, technical knowledge, and attention to detail throughout the writing process.

I am extremely grateful to Hao Ge for his support. At no benefit to him, he

offered me countless hours of help with modelling, idea generation and mathematics. I could not have attained the knowledge of induction motor fundamentals required for this project without his expertise and generosity.

Finally I would like to thank my family. Thank you to my parents for their never ending support and guidance, I owe my achievements to you. Thank you Aidan, for being my best friend. To Carly, for being my inspiration and motivation, may my achievements be a reminder that you can do anything you set your sights upon. To Bridget, for being a living, laughing testament to my mom's passion for work and family, and for reminding me always that love is the most important thing.

Contents

List of Figures

Chapter 1

Introduction

1.1 Motivation

There are more than 80 million vehicles are manufactured worldwide each year, and these numbers are expected to continue rising. With the majority of these powered solely by internal combustion engines, which have an efficiency of 20% to 30%, research has increased in order to reduce the CO_2 emissions they produce [1]. Many countries, including the United States, have created new standards for their vehicle manufacturers. Goals for the year 2025 to have an average fuel economy for passenger vehicles reaching 4.3L/100km cannot be met through the improvement of internal combustion engines alone. The implementation of electric motors to work alongside internal combustion engines in hybrid vehicles, or independently in electric vehicles, is necessary to meet these targets [1].

Invented in 1888 by Nikola Tesla, the induction motor remains the most widely used electric motor across various applications today [16]. There are many advantages to an induction machine, such as easy maintenance, low size, low weight, and low rotor

inertia. However, there is one distinct disadvantage: the speed of an induction motor cannot be continuously varied without additional equipment and the motors nature as a dynamic, non-linear system makes its control considerably more difficult than in direct current (DC) machines [16].

Permanent magnet synchronous machines (PMSM) are the most commonly used motor in the automotive industry, appearing in the Toyota Prius, Nissan Leaf, Chevrolet Volt and other modern day hybrid and electric vehicles. These machines are seen as the solution to electrifying transportation, with advantages in performance and efficiency from the magnetic field of their rotor mounted permanent magnets. However, side-by-side comparative studies [17] reveal that similar size and topology induction machines are capable of competitive performance. Additionally, since they do not make use of rare-earth metal magnets they are much cheaper to assemble and manufacture. This may become increasingly advantageous as the worlds supply of rare-earth metals may be limited [17]. Spikes in the prices of certain rare earth metals have been reported throughout the last decade due to concerns over availability of the materials [18]. The extraction by mining and refining process of rare earth magnets is not without its share of environmental concerns and accounts for 25% of the greenhouse gasses emitted by materials in an average permanent magnet machine, despite being a much smaller portion of the machine's mass [18]. The merits of induction machines, which do not make use of rare earth magnets, have been harnessed by industry leader Tesla Motors, with the most envied and praised electric sports car on the market.

Induction motors are incredibly difficult to benchmark due to complicated control schemes. Each of the infinite points under the torque vs. speed curve can be achieved

with infinite current and slip combinations. Each of this combinations will have its own efficiency. How then, does one compare the efficiency maps of two machines with infinite efficiency maps. In the absence of knowing the control scheme used, a method of comparing the maximum efficiencies at each point is required.

Bar Windings are cheaper to manufacture and offer improvements in the low speed range to thermal performance and copper losses due to considerably higher slot fill factor. They are currently widely used in permanent magnet machines including the newer GM models [13] [15] [14]. A bar winding induction machine offers the low cost benefits of fully automated manufacturing and containing no rare earth metals, but must be designed to reach comparable torque and efficiency specifications to a stranded winding machine in order to be competitive. The efficiency of bar wound motors may be higher at low speeds due to high copper area and low resistance. However, efficiency of the machine is limited at high speeds by copper losses due to eddy effects in the stator windings[5] [12] .

Tesla Motors' public patents reveal 6 winding layouts that may be used in their model S vehicle's induction motor. This project aims to select the preferred or most feasible winding layout and model a motor with similar geometry to the Tesla machine, as well as match its performance capabilities. With the results in mind, a comparable bar winding scheme will be designed and implemented for a comparative analysis.

1.2 Contributions

The major contributions of this work are as follows:

1. The creation and implementation of an optimal operating point selection

scheme for an induction motor that can be used to produce an efficiency map with much lower computation time and minimizes required input current required for desired output torque. The scheme is verified by comparison to several simulations over its operating range and comparison to literature review, and estimates efficiency with 0.3% error compared to simulations.

2. Modelling and simulation of an induction motor with stranded windings based off the Tesla Motors patents [19] [20] [21] [10] [22] [23].

2. Application of the algorithm to an induction machine for traction applications which matches the performance specifications of the Tesla Model S 60 motor.

3. The design, modelling and simulation of an induction machine with solid stator windings. Geometry for the machine presented is mostly unchanged from the stranded winding motor to allow the focus of analysis to be the advantages and disadvantages of stator bars without affecting the results with other machine design analysis.

4. A comparative analysis of the two machines focused on losses and efficiency.

1.3 Thesis Outline

This thesis begins with a study of induction motors and their place in transportation electrification. The review begins with an overview of transportation electrification and broad range of electrified vehicles and powertrains on the market today. More specific information on electric motors including induction machines is then provided. The focus of the latter half of the chapter is analytical methods of calculating torque, power, and losses as well as an in depth look at stranded stator windings.

Chapter 3 is a literature review of available information on the Tesla Motors' induction machine found in the 2013 Tesla Model S vehicle. Beginning with reviews of

the car, comments on the powertrain and performance, and a look at its market share which highlights the importance of studying the motor. The next section takes a more in depth look at the performance specifications for the induction motor. The last two sections of chapter 2 describe the geometry and winding layout of the representative motor created in ANSYS Maxwell for this thesis.

Chapter 4 outlines the proposed method and optimization algorithm for generating an efficiency map for an induction machine based on simulation data. An initial method of generating equivalent circuit parameters based on data is reviewed and applied to the representative motor from chapter 3. The major shortcomings of this procedure are the inability to incorporate core losses, which vary with excitation frequency as well as slip frequency. Section 4.2 describes a major contribution of this thesis, the proposed algorithm which creates an efficiency map with much fewer simulations and computational effort than would be needed otherwise. The method depends on d-q axis analysis which is briefly explained before the proposed optimization equations are given. The step by step procedure is then outlined before it is applied to the representative motor in section 4.3. In section 4.3 the efficiency map as well as a loss contour plot can be seen for the representative motor. The chapter concludes by validating the proposed algorithm in two ways: by comparing calculated results with simulation data at points that were not used in setting up the efficiency map, and by comparing to an efficiency map for the Tesla Motor completed in another study by Motor Design Ltd [9].

Chapter 5 provides a description of bar windings and the concerns they create for a motor designer. First, the potential performance advantages are outlined and then the performance disadvantages, in the form of eddy currents, are described.

Additionally, some factors that may affect the eddy currents such as slot depth, slot opening size and the number of stator bars per slot are highlighted.

Chapter 6 brings about the design of a bar wound motor for comparison with the representative motor. The motor described and modelled has very few changes from the representative motor to allow for maximum comparison. The goal is not to present a new or improved motor, but to study the efficiency map of similar motors with both stranded and bar windings. The algorithm from chapter 4 is then applied to the bar wound motor and the resultant efficiency map presented. The chapter briefly reinforces the proposed optimization algorithm by validating its results for a second motor. Chapter 6 concludes with a comparative analysis of the bar wound and stranded wound motor where the losses and efficiency are highlighted. The similarities in the form of flux density profiles, torque speed profiles and core losses are shown, and the major difference between the motors in the form of eddy currents. Finally, the efficiency maps are compared and the impact of the eddy currents on the overall efficiency is clear.

The thesis concludes in Chapter 7 where the accuracy and benefits of the optimization algorithm are summarized; the results of the comparative analysis are summarized; and suggestions are given for future research.

Chapter 2

Induction Motors for Electrified Powertrains

2.1 The Call for Transportation Electrification

There are a range of vehicles considered electrified. In fact, nearly every vehicle on the road today makes use of a battery and electric motor for starting, air conditioning, vehicle lights, radio and alternator, but the energy provided for propulsion comes from the internal combustion engine (ICE). Figure 2.1 shows the percentage of energy derived from gasoline and the percentage of energy derived from electricity (the vehicle battery) in a wide range of vehicle styles. In a hybrid vehicle (HEV), the electric motor also contributes to the propulsion of the vehicle, rather than simply for starting and passenger comfort. The battery in an HEV is charged from the engine as well as regenerative braking. In a plug-in hybrid electric vehicle (PHEV), propulsion is provided by both an electric motor and an ICE but the vehicle battery can be charged by the grid. This means that a PHEV has the ability to drive using only

electric propulsion for a portion of its range. A battery electric vehicle (BEV) is driven solely with the electric motor powered by the battery, which is charged from the grid, there is no fuel tank and no ICE [1].

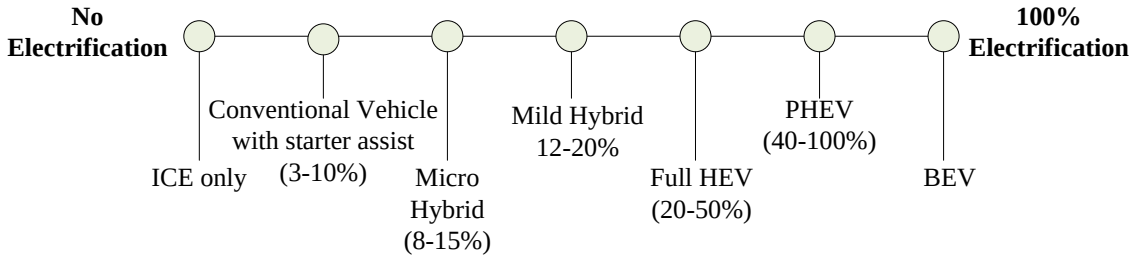

Figure 2.1: Levels of vehicle electrification showing the degree of electrification in various vehicles on the road today [1]

With the cost and environmental impact of gasoline powered vehicles, and the relative efficiency of electric motors vs. internal combustion engines (ICE) in mind, the author presents a rudimentary argument that a higher level of electrification is always desirable, barring factors like vehicle range and performance. However, the question is raised: where does the electricity come from?

This brings about the concept of source to wheel efficiency - comparing the efficiency of ICE vehicles and BEVs including every step from mining of natural gas to the efficiency of the drivetrain [24].

Figure 2.2 shows the source to wheel efficiencies of a traditional gasoline vehicle and a BEV assuming the energy comes from an equivalent natural gas source [2]. In reality, the outcome for an BEV may be even better considering that a portion of the energy may come from renewable energy sources like solar and wind or from nuclear power.

In [2] the information in Figure 2.2 is presented based on theoretical values alone, however, actual reported efficiency ranges were also given. In order to make a fair

comparison the most efficient reported values are used for the preparation of Figure 2.2.

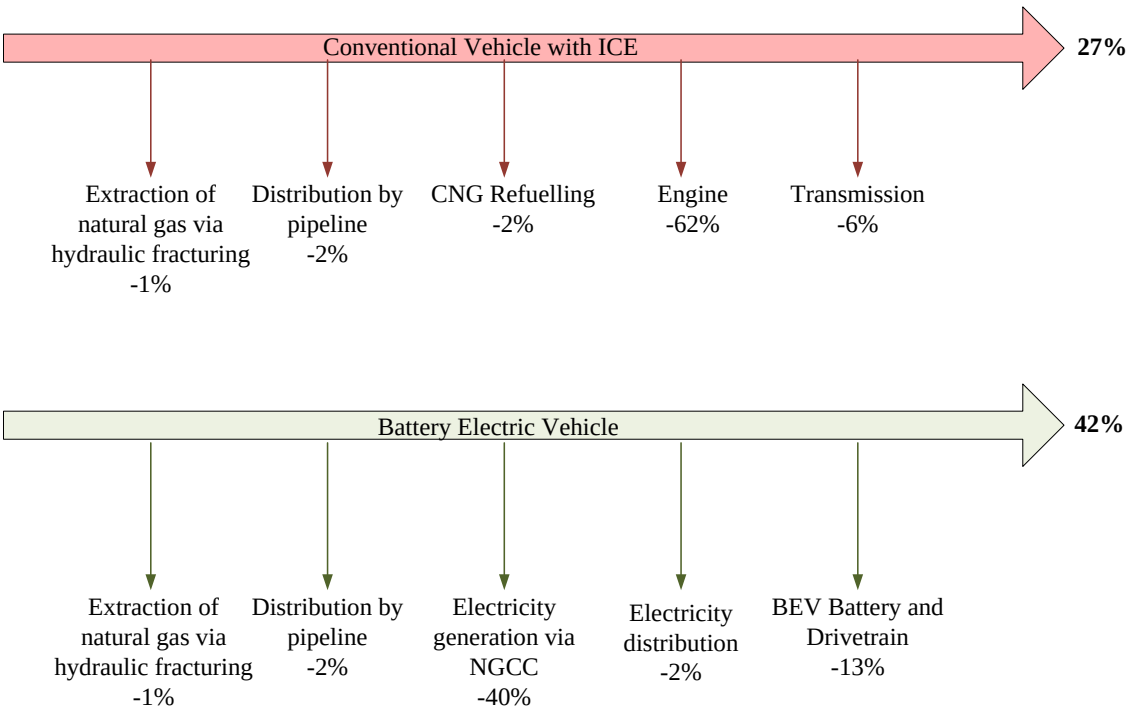

Figure 2.2: The major sources of losses in the source-to-wheel efficiency calculations for conventional vehicles and BEV [2]

The losses in the pipeline only account for the compression, as it is impossible to estimate how far the gas will have to be pumped or transported to the processing plant. The comparison fairly assumes that both the compressed natural gas (CNG) refuelling centre and the natural gas combined cycle (NGCC) electricity plant are located at the site of extraction.

A study of all forms of electricity vs. diesel and gasoline engines in Europe was performed in [25]. Their conclusions are that a gasoline vehicle is at best 18% efficient and at worst 11%. While the paper states that an electric vehicle powered by electricity from coal may also be only 18% efficient, a potential of 57% efficiency,

well-to-wheel, if renewable energy is used.

The theoretical maximum is calculated with concepts including the ideal Carnot cycle for NGCC power plant efficiency, and the ideal Otto cycle for the ICE. The BEV clearly surpasses the gasoline car in efficiency even when considering the production of electricity. Further engineering of the BEV will be the preferred pathway to achieving maximum vehicle efficiency, potentially as high as 84% with natural gas as the original fuel source according to [2].

2.2 Electrified Vehicle Powertrains

A typical electric vehicle powertrain looks much like a conventional gasoline vehicle's powertrain. The fuel tank and ICE are replaced by a battery pack traction motor, respectively [3]. The other components of the powertrain are the control unit, a battery management system, converter, inverter and regenerative braking system [26]. A typical BEV powertrain layout is shown in figure 2.3. The functions of the battery and motor are to store energy and to convert electric to mechanical energy, respectively. The functions of the remaining components are summarized in this section.

Converter: A DC-DC converter generates an output voltage as specified by a control system from a battery voltage. Without a dc-dc converter the battery output voltage may limit the vehicles maximum power. Dc-dc converters allow for flexibility in system design and easier control of the motor. The converter may be one of several types: buck, boost, or buck-boost [5].

Inverter: The inverter is responsible for changing a DC-voltage source, which is what is available directly from a vehicle battery in some systems or from the DC-DC

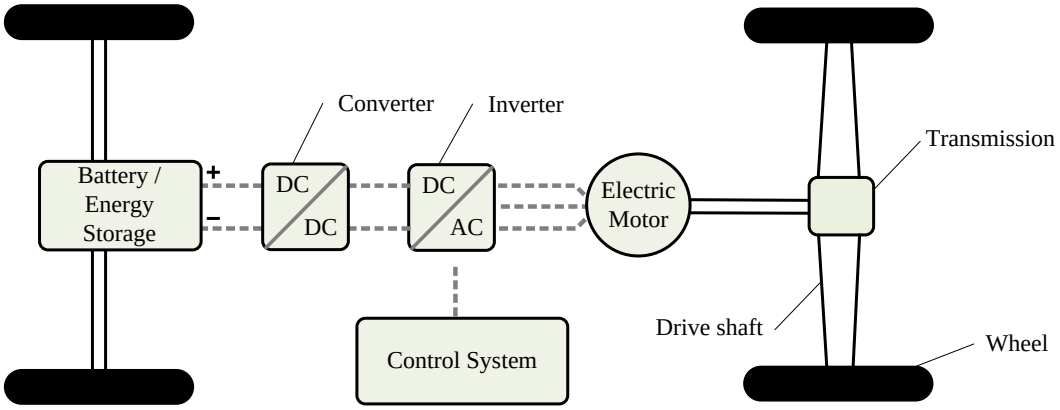

Figure 2.3: Typical electric powertrain layout [3]

converter in others, into a three phase alternating current (AC) voltage. Once again the controller will specify a desired parameter, in this case frequency, and the output voltage is changed to a 3-phase AC-voltage at this frequency [5].

Both the inverter and converter have inherent losses, which contribute to the efficiency of the vehicle. Converters are also responsible for choppy voltages or current ripple which may cause additional harmonics in the motor and therefore increased motor losses [5]. It is important to note that this thesis focuses solely on motor efficiency and does not include these types of losses in its results.

ECU: The electric control unit is responsible for taking driver input (break and accelerator) and specifying the desired voltage and frequency to the converter and inverter [5]. This thesis does not focus on the actual control system applied to the representative motor, but an ideal one. The frequency and voltage chosen for each operating point are those which maximize efficiency. While ideally a vehicle could implement this control system - the actual controls used are likely much simpler.

2.3 AC Electric Machines

Electric machines are devices that convert electrical energy to mechanical energy in a motoring mode, or mechanical energy to electrical energy when in a generating mode. There are three types of machines which convert an AC current to mechanical power. These are Switched Reluctance Machines (SRM), Permanent Magnet Synchronous Machines (PMSM) and Induction Machines (IM). Each motor concept has its merits. A PMSM is capable of higher power density, but it is also more expensive and not capable of high efficiency at high speeds. PMSM achieve higher efficiencies because of their much lower copper losses, due to the copper rotor bars in an IM. However, at high speeds an PMSM is subject to field weakening and are outperformed by IM [27]. A SRM may be capable of comparable power density and efficiency to an induction machine, as well as better thermal performance [28]. However, SRMs are not practical in vehicles due to their high torque ripple and acoustic noise. Figure 2.4 shows the most efficient areas for each motor. The parts of the torque vs. speed curve where each motor is capable of an efficiency higher than 85% is outlined.

The figure shows that the PMSM is capable of achieving high efficiency at the highest torques. However, the figure does not resolve a debate between PMSM and IM. In high speed applications, such as highway driving, the IM offers better efficiency.

It is also suggested in [4] that the choice of motor in a hybrid vehicle may also depend on the hybrid configuration. For example, a series hybrid system requires maximum vehicle power over the entire speed range, making an IM a good choice. In a parallel hybrid system, the speed range may depend on gear selection and is often restricted to lower speeds making a PMSM more appropriate.

The study in [4] focused mostly at the efficiency map to draw conclusions, which

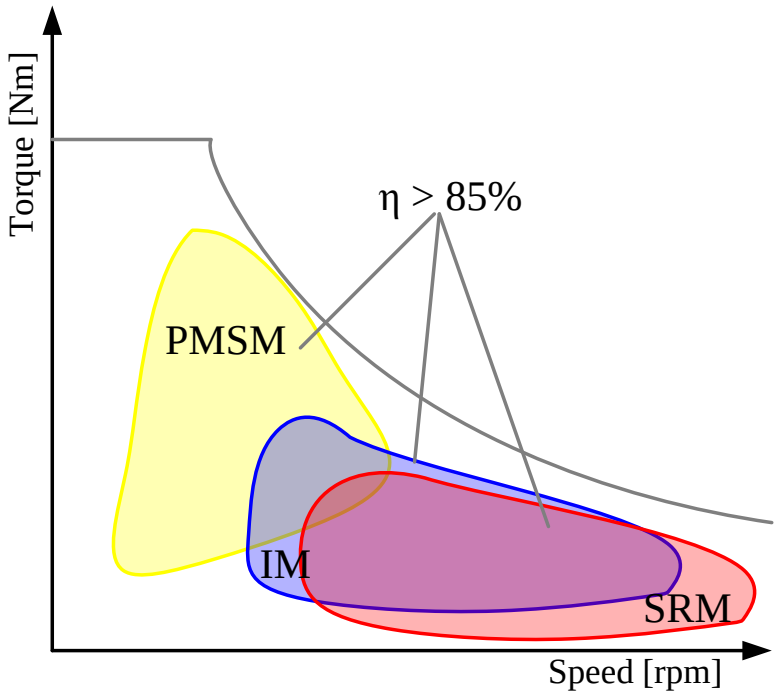

Figure 2.4: Comparison of optimal operating ranges for the most commonly used electric machines as traction motors [4]

is the standard method of measuring motor performance in industry. A further study completed in [27] suggests that efficiency maps may be an incomplete method of comparing vastly different motors due to differing control strategies and due to the dynamic nature of traction machine applications. An efficiency map is perfect for comparing steady state efficiencies but not always the dynamic and transient performance of IMs and PMSMs. The two types of motors were therefore also compared over 5 different drive cycles. The authors in [27] initially confirm the common conclusation that PMSM have higher efficiencies and power density. However, they note that the nature of a PMSM means it was operating at mostly optimal points but claim that an IM is rarely studied at optimal points. Once they applied a loss minimization

algorithm they conclude that the IM performs comparably on all cycles and even better in the federal urban driving schedule (FUDS) driving cycle.

With comparable performance and the elimination of expensive and difficult to acquire rare-earth metals induction motors are a promising option in the future of traction motors for EV applications [4] [27].

2.4 Description of an Induction Machine

There are two main types of induction machines: wound rotor and squirrel cage, and the difference is in the rotor winding style. In a wound rotor machine the rotor windings are three phase similar to that of the stator. Alternatively, in a squirrel cage IM copper rotor bars are placed in all rotor slots and short circuited using end caps [28] . Figure 2.5 shows the topology of a squirrel cage induction motor, more commonly used in traction applications [29].

The name induction motor comes from the very function of the machine. Torque is generated from the force on the rotor. Lorentz's force law states that when rotor currents are short circuited, as done by the end windings, the induced current generates a force thus causing the motion of an induction machine [5]. These rotor currents are induced by the rotating magnetic field generated by the stator currents. Stator currents are usually three-phase distributed, and can be in any number of winding layouts. The strategy in selecting or designing a stator winding layout is a large part of induction motor design.

In order to induce voltage on rotor conductors, magnetic flux must flow through the closed surface of the rotor bar. This is not possible if the rotor is rotating at the synchronous speed. The synchronous speed ω_s is the speed at which the magnetic

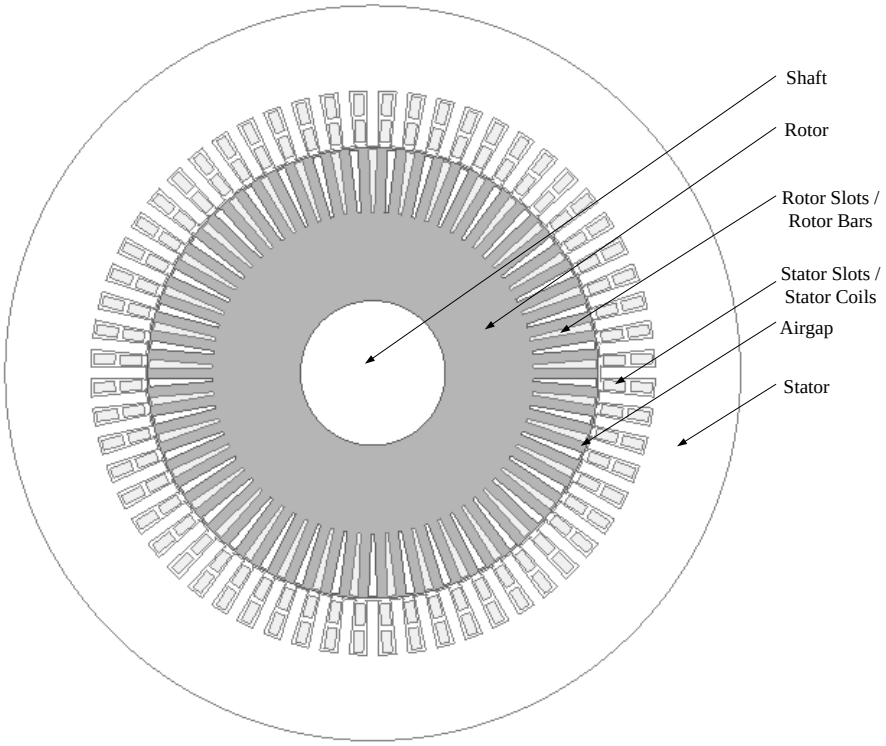

Figure 2.5: Basic geometry of a squirrel cage induction motor with components labelled.

field is rotating based on the alternating current source, it can be calculated as is done in equation 2.1 from the frequency and the number of electric pole pairs in the machine. The rotor moves at a lower speed ω_r than the electric field which induces flux and therefore torque. It may appear that the rotor is attempting to "catch up" to the synchronous speed. The difference between the synchronous speed and the actual speed of the machine is called the slip frequency or can be expressed as a unit-less fraction called slip, calculated in equation 2.2 [16].

$$w_s = \frac{60f}{pp} \tag{2.1}$$

$$Slip = \frac{w_s - w_r}{w_s} \tag{2.2}$$

When the machine is operating at stationary conditions (a slip of 1) it functions much like a transformer with an air gap, this can also be seen in the equivalent circuit model figure 2.6. As mentioned, when slip is 0, no torque is produced. When the rotor rotates faster than the synchronous speed (negative slip) the machine is generating, and when rotation is slower than synchronous speed (positive slip) the machine is motoring [5].

2.5 Equivalent Circuit and Derivation of Equations

Figure 2.3 is an equivalent circuit for an induction motor. An equivalent circuit model is useful in deriving the equations which govern a machine's ability to produce torque.

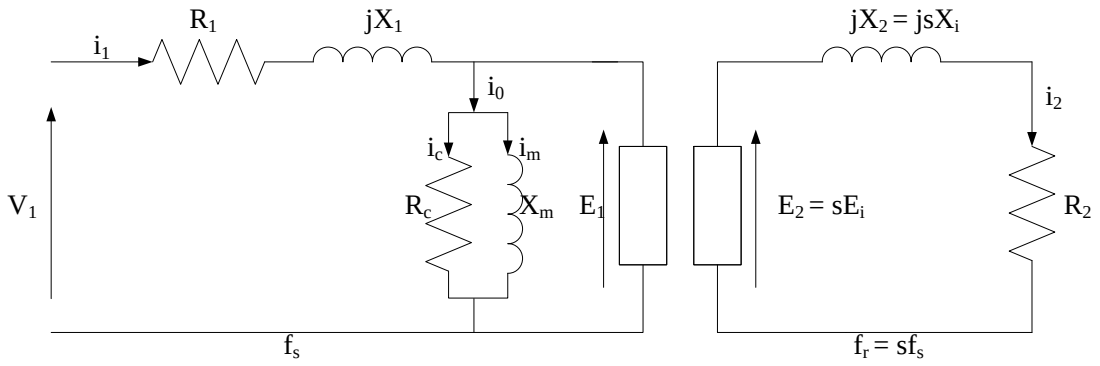

Figure 2.6: Equivalent circuit model for an induction machine [5].

The equivalent circuit model for an induction machine looks similar to that of a transformer, and has similar behaviour when the motor is stationary . The induced

voltage in a transformer (or stationary machine) E_i, and the rotor voltage E_2 in a moving induction machine are related with slip:

$$E_2 = sE_i \tag{2.3}$$

Similarly, the inductance and frequency of the rotor are calculated from the locked rotor case s=1 and the induced inductance or stator frequency [5][30].

$$X_2 = sX_i \tag{2.4}$$

$$f_r = sf_s \tag{2.5}$$

The induced rotor voltage depends on both resistance and reactance, where rotor resistance is a constant R_2 and reactance is affected by slip. The rotor reactance is given by:

$$X_2 = w_r L_2 = 2\pi f_2 L_2 \tag{2.6}$$

This equation can be easily changed to rely on slip and locked rotor resistance as shown where $f_2 = sf_1$:

$$X_2 = 2\pi f_2 L_2 = s(2\pi f_1 L_2) = sX_{locked} \tag{2.7}$$

A final note on the rotor is that the rotor current can be compared to the rotor voltage or to the locked rotor voltage with the simple voltage-current-resistance triangle. This comparison creates the two equations for rotor current:

$$I_2 = \frac{E_2}{R_2 + jX_2} \tag{2.8}$$

$$I_2 = \frac{E_{locked}}{R_2 + jsX_{locked}} \tag{2.9}$$

2.6 Theoretical Power and Losses from an Induction Machine

The efficiency of any motor is evaluated on input and output power. There are several power measurements that should be discussed when studying an induction machine. P_{in} will refer to input electrical power from the three phase current or voltage supply where power is calculated $P = VI$. Next, consider the copper losses P_{Scu} and P_{Rcu} in the stator and rotor respectively which are generated from resistance in the windings and calculated from the relationship $P = I^2R$ unless effected by eddy currents at high speeds - which is more likely in the rotor bars than in the stranded stator windings. However, it is not necessary to accurately calculate eddy current losses in the rotor to estimate output power and efficiency as will be shown later in equation 2.14. Iron losses or core losses P_{fe}, are the power lost as hysteresis and eddy currents in the stator material. In the equivalent circuit shown in figure 2.6 the core losses are accounted for with the resistor R_c, and then calculated with the same relationship as copper losses, although this is simply for ease of an equivalent circuit model and not how they are produced in the machine. Finally, once all losses are accounted for the output power of the machine is P_{out}.

$$P_{out} = P_{in} - P_{Scu} - P_{Sfe} - P_{Rcu} - P_{Rfe} - P_{mech} \tag{2.10}$$

Which leads to the machine output torque and efficiency calculated in equations 2.11. From the output vs. input power the efficiency can also be calculated, shown in equation 2.11. Stator copper and core losses may be easy to estimate from the equivalent circuit, but for rotor losses are difficult to estimate as they are more strongly affected by eddy currents. Air gap power can be calculated from P_{in} and the stator losses and from there eliminate rotor losses by grouping them together and creating a simpler relationship based on slip as shown in equations 2.13 and 2.14 [5] [30]. Air gap power can be simulated in finite element analysis by looking at flux in the air gap. Figure 2.7 summarizes where P_{in} P_{out} and P_{ag} can be measured as well as where the different losses as generated in the motor.

$$\tau_{out} = \frac{P_{out}}{w_r} \tag{2.11}$$

$$\eta = \frac{P_{out}}{P_{in}} * 100\% \tag{2.12}$$

$$\eta = \frac{P_{ag} - P_{Rcu} - P_{Rfe} - P_{mech}}{P_{in}} * 100\% \tag{2.13}$$

Rotor losses are estimated as with an inductor, and related to slip. Therefore the simplest form of efficiency is:

$$\eta = \frac{(1 - slip)P_{ag} - P_{mech}}{P_{in}} * 100\% \tag{2.14}$$

Which doesn't require exactly calculating the rotor copper or rotor iron losses but combines them in the term $(slip)P_{ag}$.

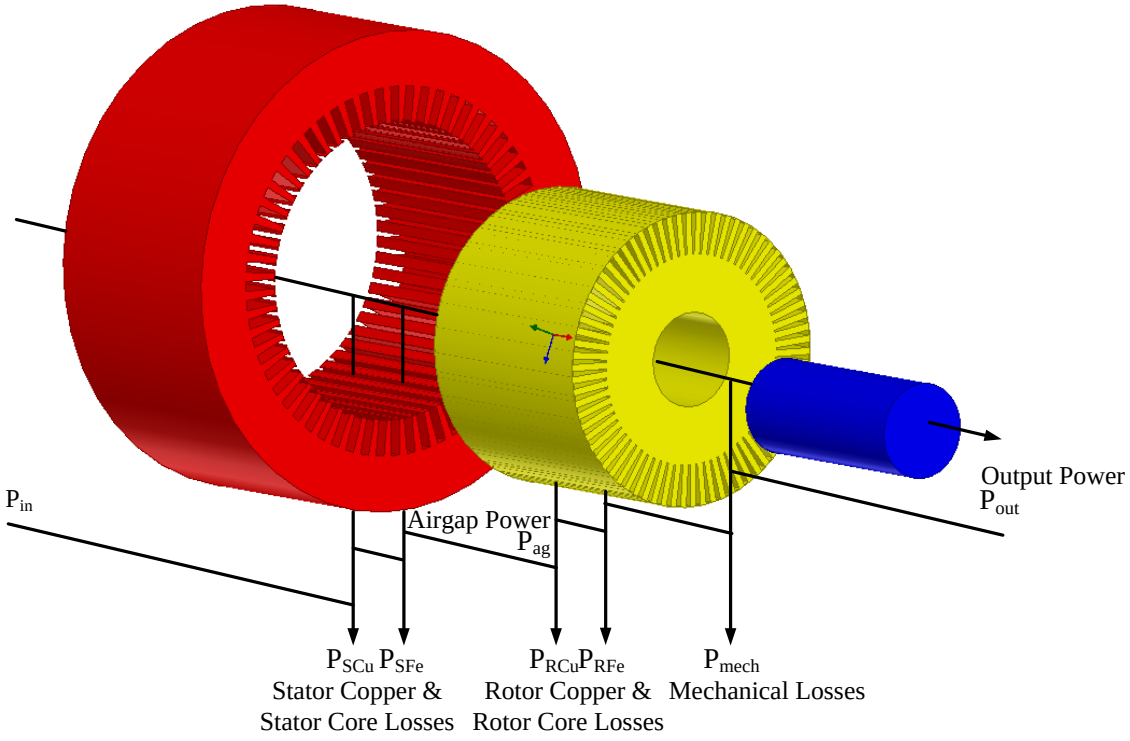

Figure 2.7: Losses and powers factors contributing to the efficiency calculations of an induction machine and their source within the motor

2.7 Stator Winding Patterns

Many of the examples and calculations in the upcoming section require the understanding of involved definitions. To quickly describe a motor the number of phases, slots and poles is often given, which quickly gives a picture of how the motor looks and works. The number of phases, which is always in multiples of 3 in an AC machine,

describes the number of different input current phases that are being applied. Therefore, with one AC current source, or one Wye connection, a machine is described as a 3 phase machine.

The number of poles is describes the number of magnetic poles in a machine which can be observed by looking at the flux lines. This also relates to the number of phases because how each AC current phase is orientated in the geometry determines the number of poles. For example, if a single phase appears twice (once in each direction) around the circumference of the motor, 180 degrees from its opposite polarity, this creates a 2-pole machine. Poles always exist in pairs since the current must appear run in a positive and negative polarity, therefore the number of poles is always a multiple of 2.

Lastly, the number of stator slots is included which immediately gives a picture of the number of slots occupied by each phase.

2.7.1 Concentrated and Distributed Windings

Consider a 3-phase, 4-pole machine. In this case, should each phase have one and only one slot per pole, this would be a concentrated winding layout. A distributed winding layout depicts one which has greater than one turn per stator slot. Due to phasor sums, the induced emf is higher in a concentrated winding layout. However, the harmonics and noise are lowered in distributed windings and the waveform is more sinusoidal.

Distribution factor describes the reduction in phase voltage or emf, magnetomotive force (mmf) or flux density caused by distributed vs. concentrated windings [5] [31]. In figure 2.8 concentrated windings are displayed in a) and distributed in b). The

distributed winding in this case has a single phase occupying three slots spaced θ radians apart. In the flux density plot the same peak value is reached but the overall flux, or the area under the curve, is lower for the distributed winding.

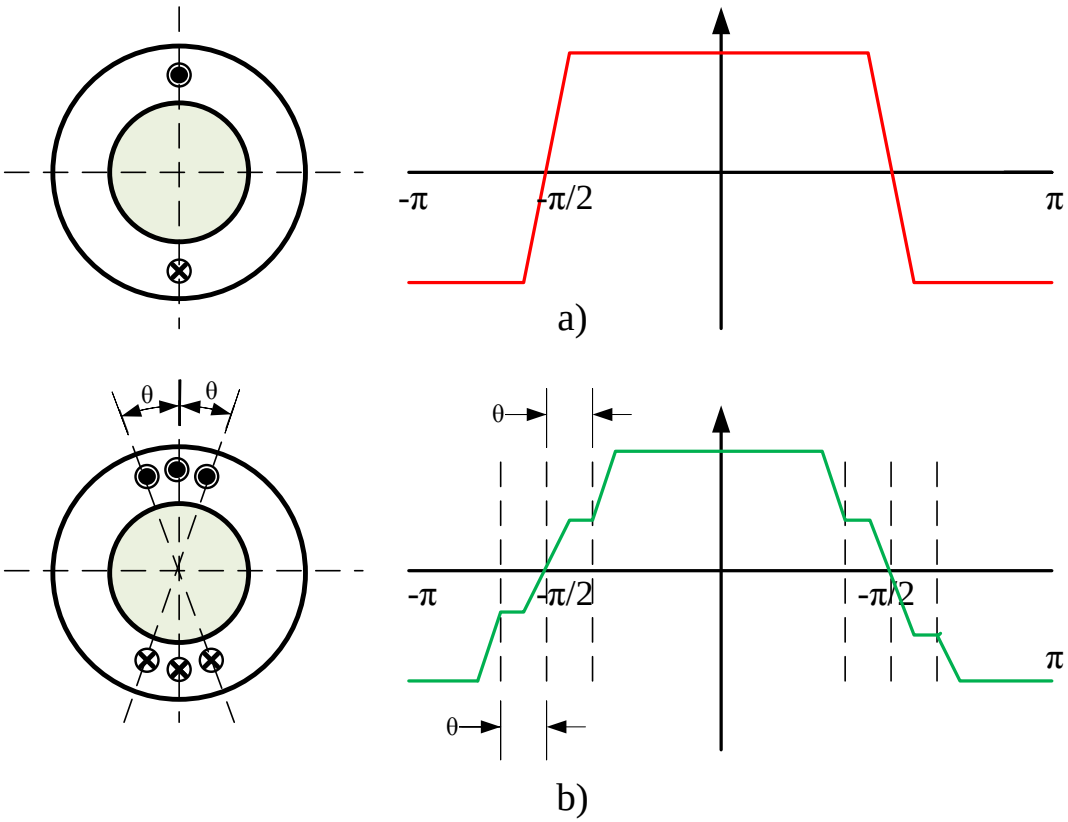

Figure 2.8: Currents with polarity shown for one phase on a a) concentrated and b) distributed winding. The figures on the right are the associated plots for flux density. [6]

$$K_d = \frac{sin(q(\theta_e/2))}{qsin(\theta_e/2)} \tag{2.15}$$

2.7.2 Double and Single Layer Windings

A second way to categorize stator windings is by the number of layers. In a single layer winding layout, each slot contains one side of one coil. This can be either distributed or concentrated. In a double layer winding each slot contains one side of two coils. Whether these coils are of the same phase is described in section 2.7.3. An advantage of double layer windings is that it allows the designer more options such as short pitching [5] [32].

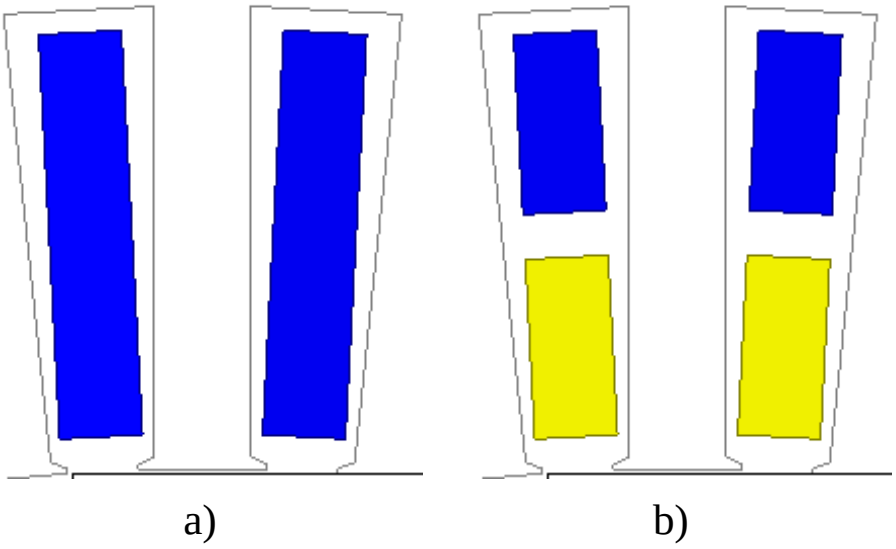

Figure 2.9: Two slots as would be seen in a) a single layer stator winding layout b) a double layer stator winding layout

2.7.3 Full Pitch and Short Pitch Windings

Consider a 4-pole machine with 60 stator slots.

$$PolePitch = \frac{NumberofSlots}{NumberofPoles} \tag{2.16}$$

For the machine in question we get a pole pitch of 15. This number corresponds to the coil span in a full pitched winding layout. Any layout with a coil span of less than 15 is considered short-pitched. There is a trade off when considering full pitch and short pitched winding layouts. The designer must compromise between total induced electromotive force (emf) and the harmonic distortion. A coil span of 2/3 of the pole pitch, in this case 10, will create the lowest emf and mmf but will eliminate the 3rd, 9th, 15th etc. harmonics. Eliminating these harmonics will make the motor more efficient and limit the torque ripple, but will compromise the maximum torque [33] [4].

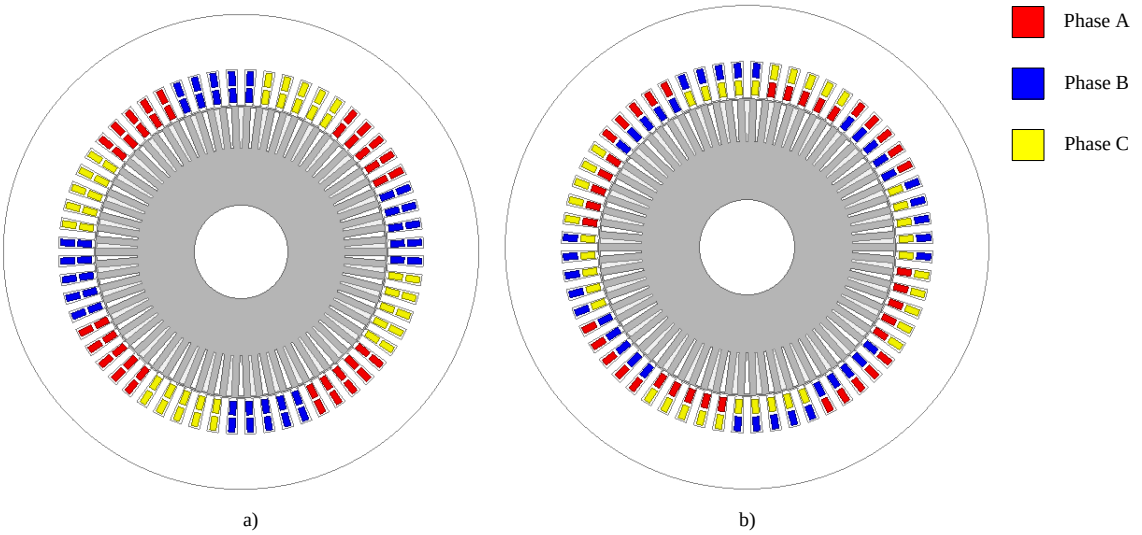

Figure 2.10: a) a 4-pole, 60-slot, double layer induction motor with a full pitch stator winding layout, coil span 15 b) a 4-pole, 60-slot, double layer induction motor with a short pitch stator winding layout, coil span 10

The maximum emf is reduced due to the phasor sum of the componenents [33]. In

figure 2.10 a) the emf induced in each phase can be found by adding the emf induced by each layer. However, in the short pitching example 2.8 b) the same phase coils are separated by 60 degrees and therefore must be added as vectors. The result will be that of the full pitch winding multiplied by a factor of $sin60$ or 0.866. 0.866 is known as the winding factor for this particular layout and the term describes the decrease in total induced emf for a short pitched motor.

$$K_s = cos(\frac{CoilSpan}{2}) \tag{2.17}$$

Winding factor, the total lost emf from a winding layout, accounting for short pitching and distributed windings is the product of the distribution factor and pitch factor.

$$wf = K_d K_s \tag{2.18}$$

2.8 Evaluating Motor Performance

Two characteristics that make an electric motor viable for EV applications are a wide speed range and a wide torque range. A wide speed range is necessary for the car to reach high speeds. Motor performance at very low speeds contribute to driver comfort, since at low speeds torque ripple can be high creating a jerky ride. Performance at low speeds is also important for safety in situations like starting on hills [5].

A wide torque range is important since the driver will at times dramatically accelerate or dramatically decelerate. The motor must be able to efficiently and stably hold its maximum torque when the driver accelerates over a period of time, for the

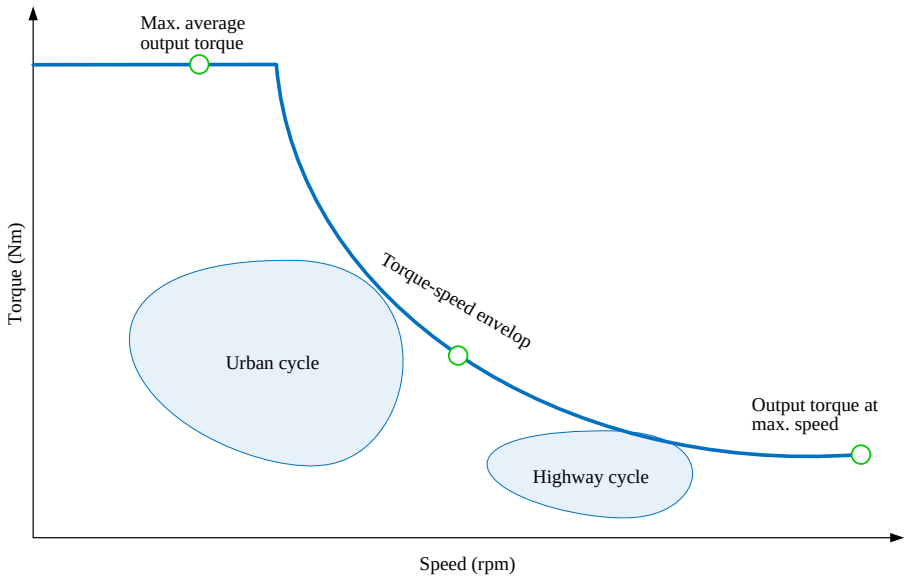

Figure 2.11: Priority operating points of an electric motor for traction applications labelled [3]

entire period of time. The motor's low torque capabilities have a strong effect on the regenerative braking system's efficiency [5].

It is valuable to study the efficiency map over the entire torque-speed range, a contour plot of efficiency under the torque speed envelope is a preferred way to study a motors overall performance [34] [35]. Efficiency maps are able to represent efficiencies of large complex systems, the motor is treated as a black box with a single output for given inputs. In an efficiency map it is assumed that the inputs have been optimized for the best efficiency at a Torque/Speed point. For induction machines this optimization is usually done by balancing flux and current for maximum efficiency [34] [35]. Figure 2.11 shows the shape of a typical torque speed envelope and priority operating points. The highest torque and highest speed, highlighted in green bubbles should be noted as discussed above, both will be required at some operations for the

motor. The shaded regions within the map are important because they are the most used operating points for their respective drive cycles — so overall motor efficiency depends largely on the efficiency in those regions. It can be noted from figure 2.4, that the most efficient points for an PMSM correspond to the urban cycle, and the IM align more with the highway cycle.

Chapter 3

Representative Electric Traction Induction Motor

3.1 Tesla Motors

The Tesla Model S was the second most popular electric vehicle sold in Canada in 2016 as can be seen in Figure 3.1. The other two Tesla vehicles sold make Tesla Motors the most popular manufacturer of electric car in the country. Of the notable cars sold, only the Tesla Motors vehicles make use of an IM rather than PMSM, making this the induction motor to beat in industry.

Despite higher sales, the Nissan leaf delivers lower maximum torque and lower maximum power than the Tesla Model S. Tesla Motors has stood apart from the competition and is often regarded as the vehicle that changed the public perception and enthusiasm about EVs [36] [37]. In [36], a description of the many innovations of Tesla Motors is presented, including notable battery and infrastructure development. However, the performance specifications of the Tesla motor are undeniable and make

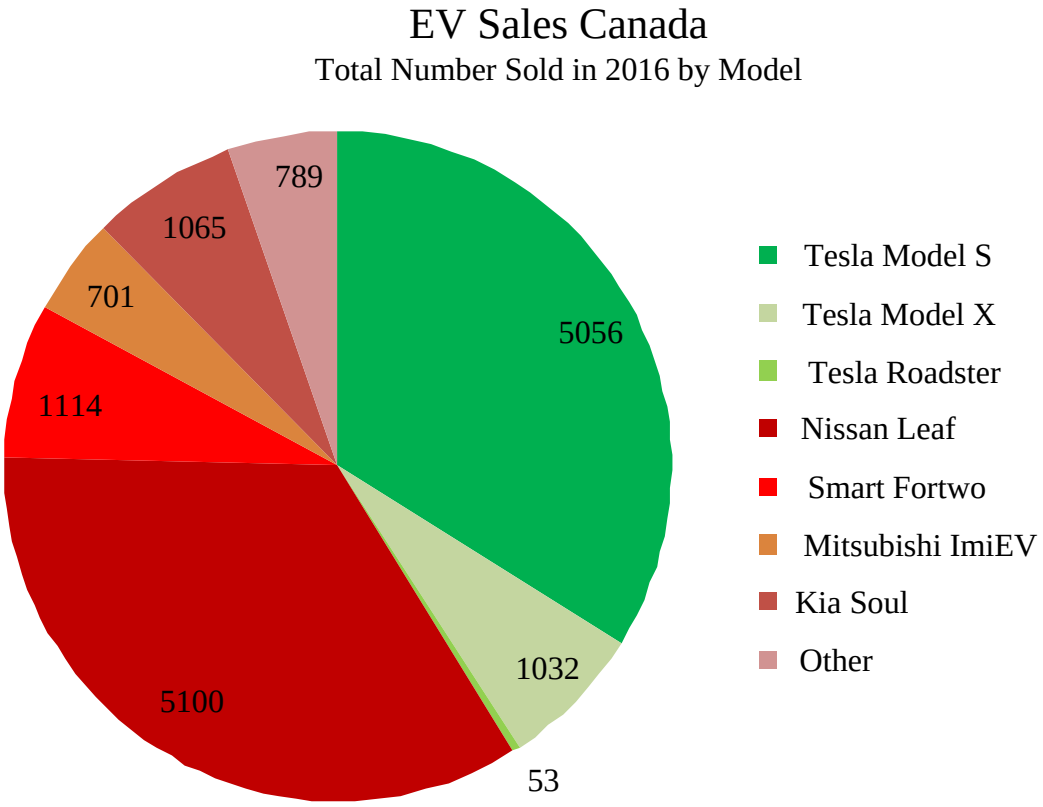

Figure 3.1: Number of BEVs sold in Canada in 2016 [7].

Figure 3.2: Tesla model S 2013, the highly rated vehicle for which the basic geometry and performance specifications are based in the representative motor. Courtesy of Car and Driver.

up a large section of their list of innovations. In order to study cutting edge technology in induction motors one must consider Tesla's machine. Over the years, Tesla has improved its battery capacity and offered new models of more affordable or higher end cars, but the motor remains largely unchanged from the motor in the original Tesla Model S. The 2013 Tesla Model S is pictured in figure 3.2 and it is its specifications used for the design of the comparable representative motor in this chapter. This chapter will present the performance specifications of the Tesla Motor which will create a ballpark goal for the representative motor design, as well as summarizing available information on the motor geometry and windings from patents, and then the selected motor geometry and winding layout for the proposed representative motor.

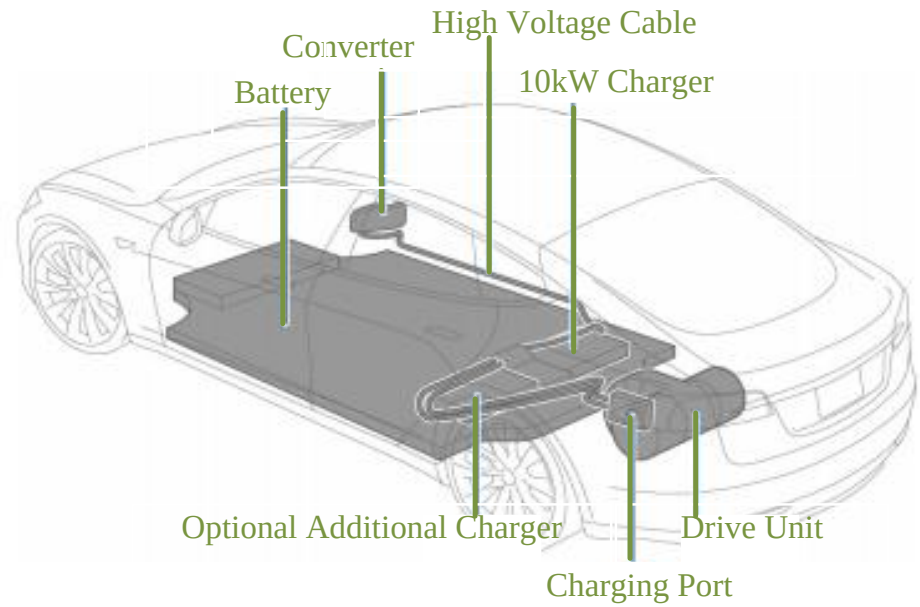

Figure 3.3: The labelled components of the Tesla motor which contribute electric power to be used in the motor. There will be other electric components in the vehicle used for lights, radio, AC, etc. but these are not relevant to the motor and as part of a low voltage system [8].

The motor does not operate in an isolated environment but rather as part of a larger interconnected system. Figure 3.3 shows the high voltage components of the vehicle, in other words, any parts used directly in the storing, transforming, or transferring of energy to be used for the motor.

Table 3.1 summarizes some parameters for the vehicle outside of the induction motor. Popular reviews of the car tell us that it has the ability to accelerate from 0-60 mph in 4 seconds and can achieve a top speed of 180 km/h [38] [39]. The challenge is to design an induction machine based on the public Tesla patents which is able to achieve this level of impressive performance.

Table 3.1: Vehicle Specifications [38] [39] [8]

Vehicle Weight	2100 kg
Overall Length	4970 mm
Overall Width	2189 mm
Vehicle Range	260 Km
Transmission	Single speed, fixed gear
Wheel Diameter	19”
Battery Type	Lithium Ion
Battery Rating	60 kWh
Battery Voltage	366 V DC

3.2 Motor Performance Specifications

In [9] an induction motor is studied which was designed based on the performance specifications and public information about the Tesla motor. The reported maximum torque for their induction machine is 430 Nm at 5000 rpm and the torque is reported as 175 Nm at a maximum speed of 14000 rpm. These numbers correspond to the reviews of the automobile on websites including Car and Driver [38] and Motor Trend [39].

The study prepared by Motor Design Ltd. [9] also offers an efficiency map created based on their predictions for the motor. This can be seen in Figure 3.3. Note that this efficiency map will be compared to the one prepared from the results of this thesis in section 4.4

3.3 Creating an Initial Motor Geometry

The motor geometry used in this study takes many features of its lamination geometry from the public tesla patents [10][19][23]. The patents offer many of the dimensions

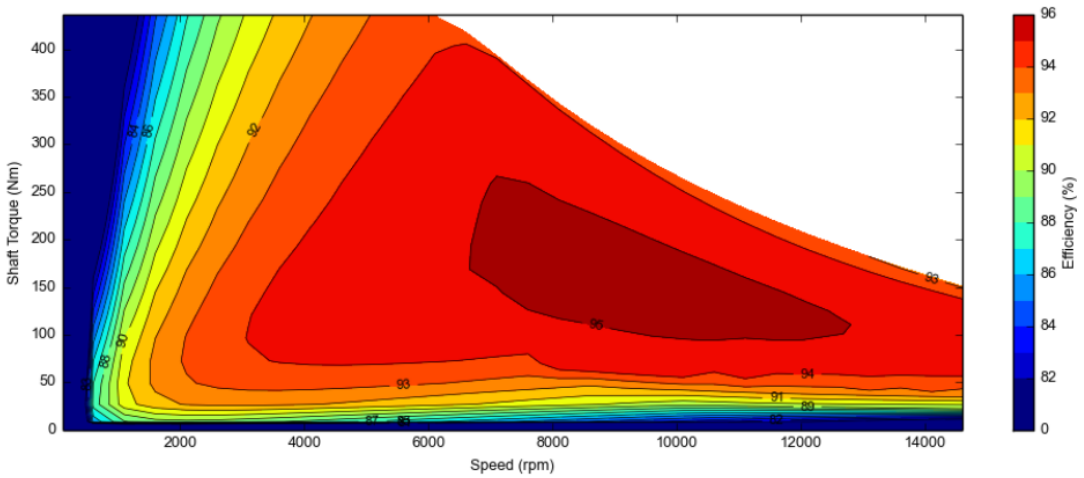

Figure 3.4: The efficiency map created in the study contucted for Motor Design Ltd. in [9]

Table 3.2: Summary of lamination geometry information in Tesla Patents [10]

Number of stator slots	60
Number of rotor slots	74
Airgap	0.5 to 0.8 mm
Ratio of stator yoke length to stator tooth width	5: 1
Ratio of rotor yoke length to rotor tooth width	5: 1
Ratio of rotor tooth length to rotor tooth width	6: 1

within a range of values or as a ratio. The most useful numerical descriptions of the lamination geometry from the patents is summarized in table 3.2. Figure 3.5 shows the basic geometry with parametrized dimensions as seen in the patents [10][23].

In [9] and [40], additional dimensions for the induction motor were presented, which were in keeping with the shape of the motor from [10] [19] and the restrictions presented in table 3.2. The dimensions used for the representative motor based on all available sources and the desired outputs are summarized in table 3.3 and presented

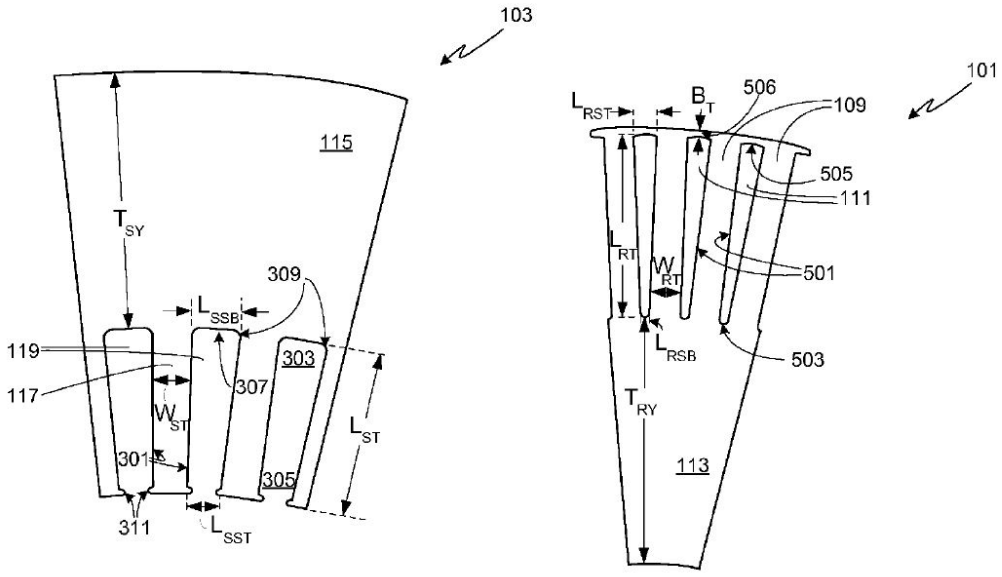

Figure 3.5: Parametrized lamination dimensions presented in Tesla patents [10].

as motor dimensions in figure 3.6 and 3.7.

The study included some additional diameters for the rounded edge of stator and rotor slots. However, to simplify the mesh and with limited effect on the motor performance the edges were squared off as is generally accepted for FEA analysis.

3.4 Creating an Initial Winding Design

3.4.1 Stator Winding Layout

Tesla's patents propose 6 feasible double layer winding layouts [20] [22] as well as one triple layer winding layout [21]. There are a mixture of concentric and concentrated winding layouts as well as a variety of pole pitches. When creating a winding layout for the representative motor it is imperative to determine and mimic the one which

Table 3.3: Summary of lamination geometry information in the Motor Design Ltd. study [9]

Stack Length	152 mm		
Airgap	0.5 mm		
Stator Information		**Rotor Information**	
Number of Stator Slots	60	Number of Rotor Slots	74
Stator Outer Diameter	254 mm	Rotor Outer Diameter	156.5 mm
Stator Inner Diameter	157 mm	Rotor Inner Diameter	50 mm
Slot Depth	19 mm	Slot Depth	23.8 mm
Slot Opening Width	2.9 mm	Slot Opening Width	0 mm
Tooth Tip Depth	1 mm	Slot Opening Depth	0.87 mm
Tooth Width	4 mm	Tooth Width	3.6 mm

has the best performance.

Each of the proposed winding layouts are double layer with three phases, 4-poles and 60 stator slots. Each has windings in 5 slot groupings with different coil span. A fully pitched winding layout in this case would have a coil span of 15, while an entirely short pitched winding would have a coil span of 10.

Evaluating the motor performance involves equivalent circuit estimation, an optimal point algorithm, and a large number of simulations. Repeating this process for each winding layout would be cumbersome and likely unnecessary. By studying the winding layouts closely the layout which will maximize the mmf without disruptive torque ripple can be predicted.

In order to achieve the very high desired output torque of 430 Nm a high winding factor is required. The selected layout is shown with a coil span of 14. This selection tends toward maximizing mmf rather than minimizing torque ripple since the reported torque of the machine is very high. The decision is therefore made based on the parameters that are available. The selected winding layout is validated by its ability

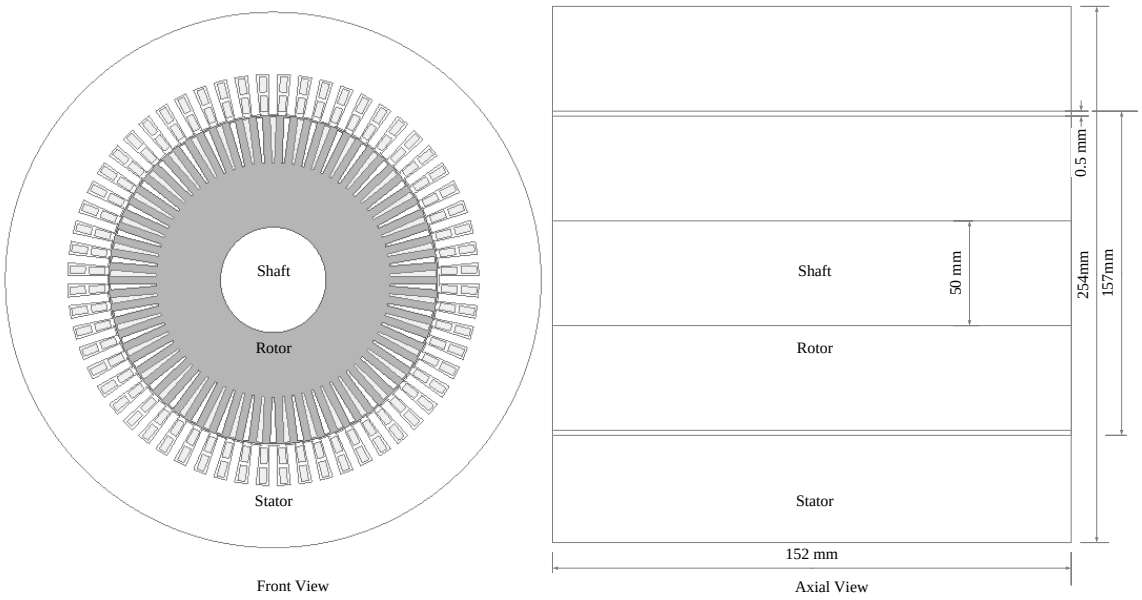

Figure 3.6: Radial and axial View of the entire motor geometry with the dimensions used for this analysis

to exactly achieve 430 Nm of torque in simulation at the limiting current as will be shown in the following chapter.

The chosen winding layout corresponds most closely with winding layout 4 in [10]. The slot numbers may differ slightly, however, based on the number of slots which are occupied by a single phase the winding factor for the proposed winding layout shown in figure 3.8 will match that of layout 4 in [10], shown in figure 3.9. In the study of the Tesla motor completed at Hanbat National University [40], a concentric winding pattern was used as in winding layout 4 from [10] however the overall coil span is 14 and the winding factor matches the one used here.

The winding factor for this winding layout is calculated below.

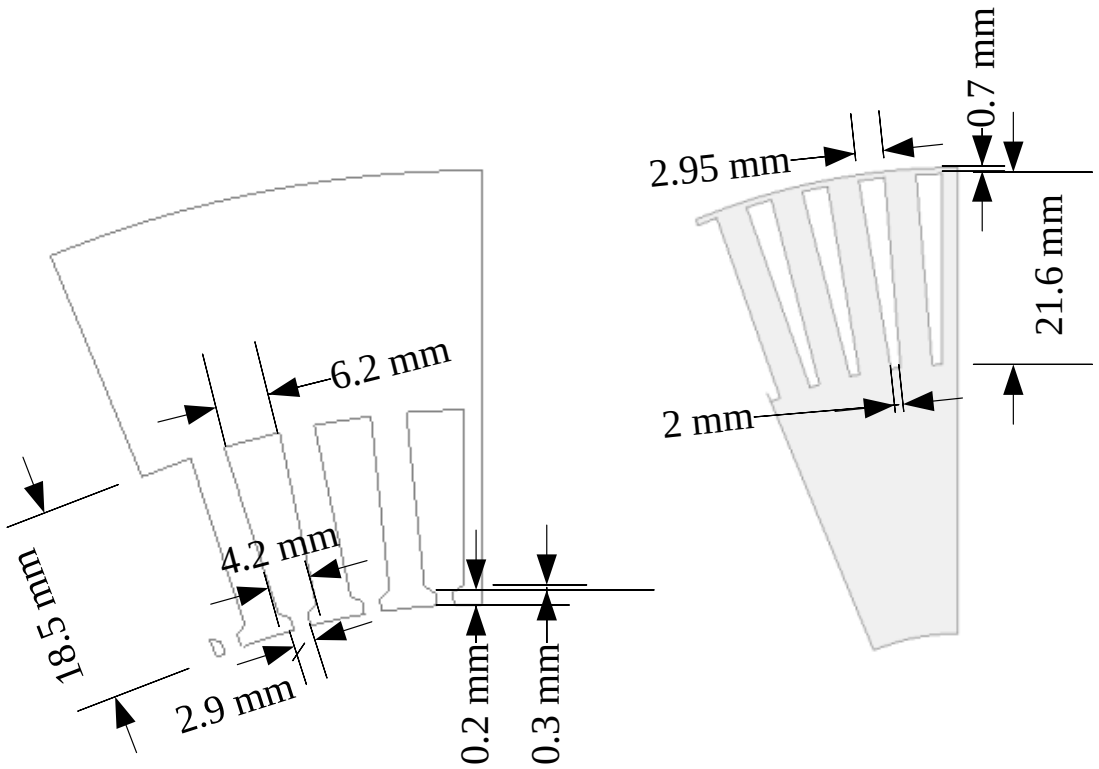

Figure 3.7: Axial view of the stator and rotor with slot dimensions as used in the analysis [10].

$$
\begin{aligned}
K_d &= \frac{sin(q(\theta_e/2))}{qsin(\theta_e/2)} \\
&= \frac{sin(5(6))}{5sin6} \\
&= 0.9567
\end{aligned}
$$

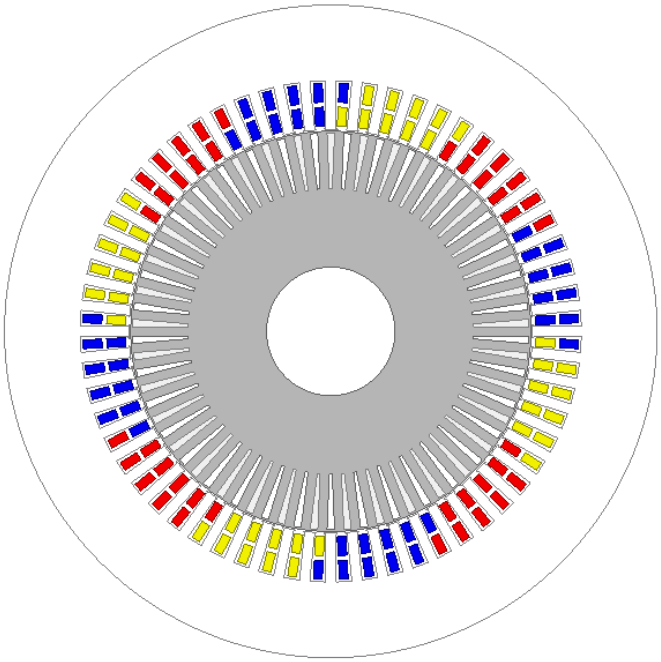

Figure 3.8: The representative motor geometry with the selected coil span of 14 where each phase is represented by a different colour.

$$\begin{aligned} K_s &= cos(\frac{CoilSpan}{2}) \\ &= cos(\frac{12}{2}) \\ &= 0.995 \end{aligned}$$

Here, coil span is referring to the angle that the machine is short pitched by. The electrical angle of one slot is 12 degrees in this case and the layout involves short pitching by only one slot.

$$wf = K_d K_s = 0.9519$$

2nd Layer (in bold & italics)

	Slot																											
	1	2	3	4	5	6	7	8	9	10	11	12	13	14	15	16	17	18	19	20	21	22	23	24	25	26	27	28	29	30
Upper	A1	A1	***C3***	***C3***	***C3***	***C4***	***C4***	***C4***	B4	B4	***B1***	***B1***	***B1***	A1	A1	A2	A2	***C4***	***C4***	***C4***	C1	C1	***B1***	***B1***	***B1***	***B2***	***B2***	***B2***	A2	A2
Lower	A1	A1	A1	***C3***	***C3***	***C4***	***C4***	B4	B4	B4	***B1***	***B1***	A1	A1	A1	A2	A2	A2	***C4***	***C4***	C1	C1	C1	***B1***	***B1***	***B2***	***B2***	A2	A2	A2

	Slot																											
	31	32	33	34	35	36	37	38	39	40	41	42	43	44	45	46	47	48	49	50	51	52	53	54	55	56	57	58	59	60
Upper	***A3***	***A3***	***A3***	C1	C1	C2	C2	***B2***	***B2***	***B2***	B3	B3	***A3***	***A3***	***A3***	***A4***	***A4***	***A4***	C2	C2	***C3***	***C3***	***C3***	B3	B3	B4	B4	***A4***	***A4***	***A4***
Lower	***A3***	***A3***	C1	C1	C1	C2	C2	C2	***B2***	***B2***	B3	B3	B3	***A3***	***A3***	***A4***	***A4***	C2	C2	C2	***C3***	***C3***	B3	B3	B3	B4	B4	B4	***A4***	***A4***

Figure 3.9: Winding layout described with slot numbers and the phase which occupies the upper and lower coil in each winding [10].

3.4.2 External Circuit and Number of Turns

For all of the proposed winding layouts, and the one created for the FEA analysis in chapter 4, the windings are connected as shown in figure 3.10. Each phase can be separated into its phase at each pole, and these are separated again into two parallel strands.

The patents also claim one turn per phase and stranded windings so it is clear that there must be multiple strands grouped together making each turn. This is discussed in patents [10] and [41]. The dimensions and number of wires were given in a parametrized method similar to figure 3.5.

A slot fill factor limit of 70% is chosen and simulated in RMxprt auto design tool, which is quite generous for a stranded winding design [5]. The final winding design consisted of 13 strands per layer per slot, therefore 26 strands per slot. The wire diameter is 1.08mm and the wire wrap thickness (individual insulation) is 0.074 mm. The dimensions for the representative can be seen clearly in figure 3.10 where they have replaced the parameterized labels from [10]. The final copper slot fill factor is 48%.

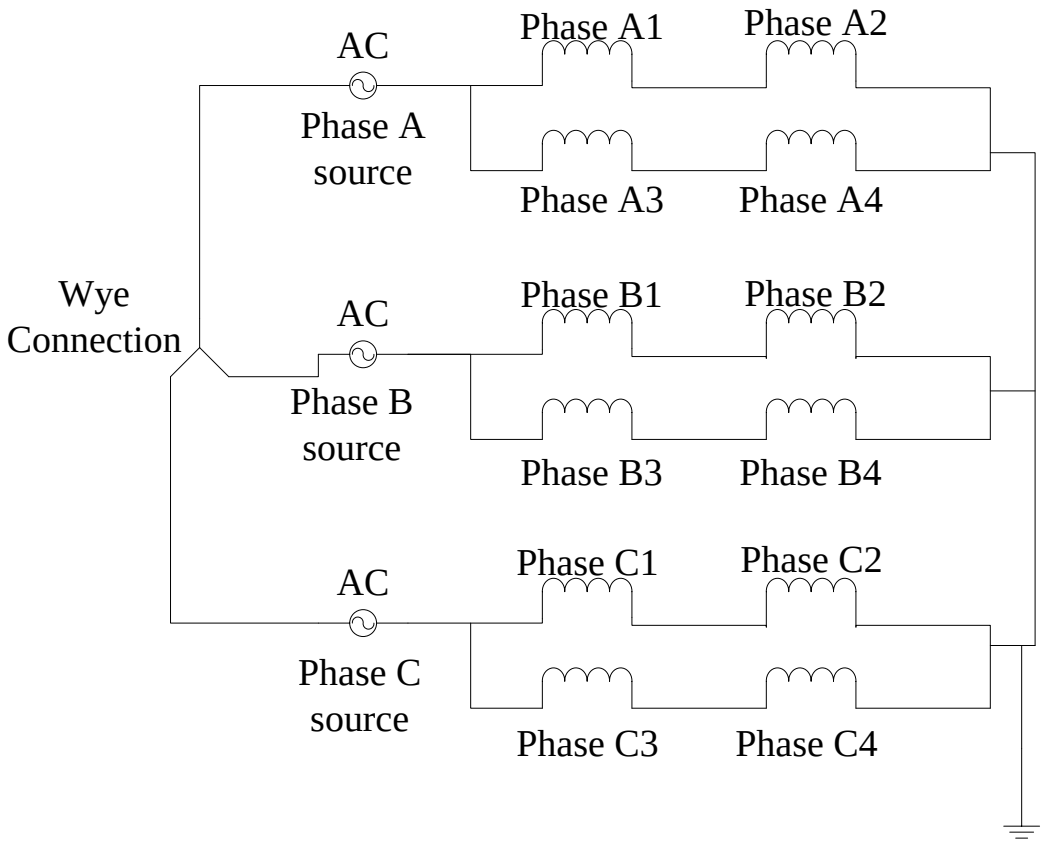

Figure 3.10: The external circuit for the representative motor [10].

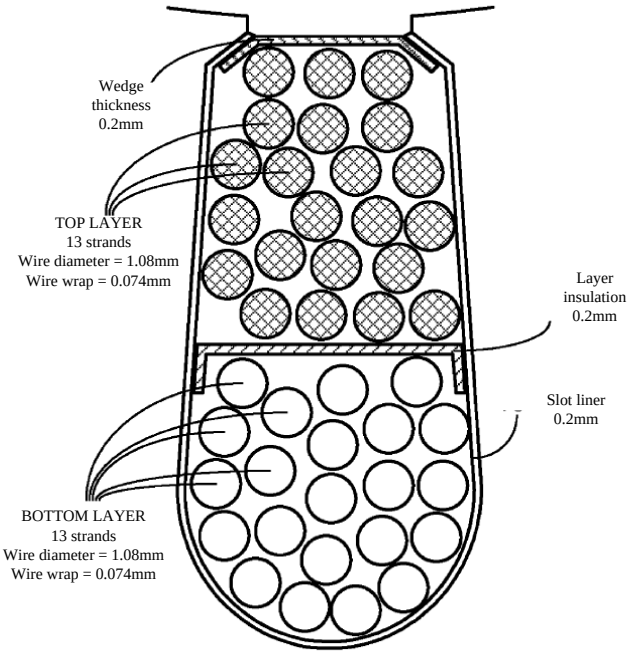

Figure 3.11: Configuration of a multiple strands, two layer slot [10].

Chapter 4

Rating Induction Motor Performance Using q-d Axis Optimal Point Selection

4.1 Equivalent Circuit Parameter Estimation

Given an induction motor geometry and winding pattern, the next step in modelling is to determine the operating conditions for the motor. This includes input voltage or current, frequency, and slip. All of these factors relate through the equation 2.1 for synchronous speed (from AC frequency of the voltage or current input), equation 2.2 for slip, and the equations for whichever control strategy is employed. The motor is capable of producing Torque at any voltage and slip combination so long as the current is less than a limiting current value and flux density is less than what is allowable on the material. The Tesla motor patents [10] include a limiting flux density on the material of 1.6 T and the study completed in [9] suggests a limiting current of 1273 A

(peak) for the stator windings. Rather than run simulations at all the possible voltage and slip requirements that meet this criteria, equivalent circuit parameter estimation is proposed in this section.

The curve fit is executed on simulation results from Maxwell ANSYS. The simulations were run at a line-to-neutral voltage value of 86.5 V_rms, which achieves the desired output Torque of 430 Nm just below the current threshold and at a slip of 0.011. The current and torque are both plotted against slip in Figure 4.1.

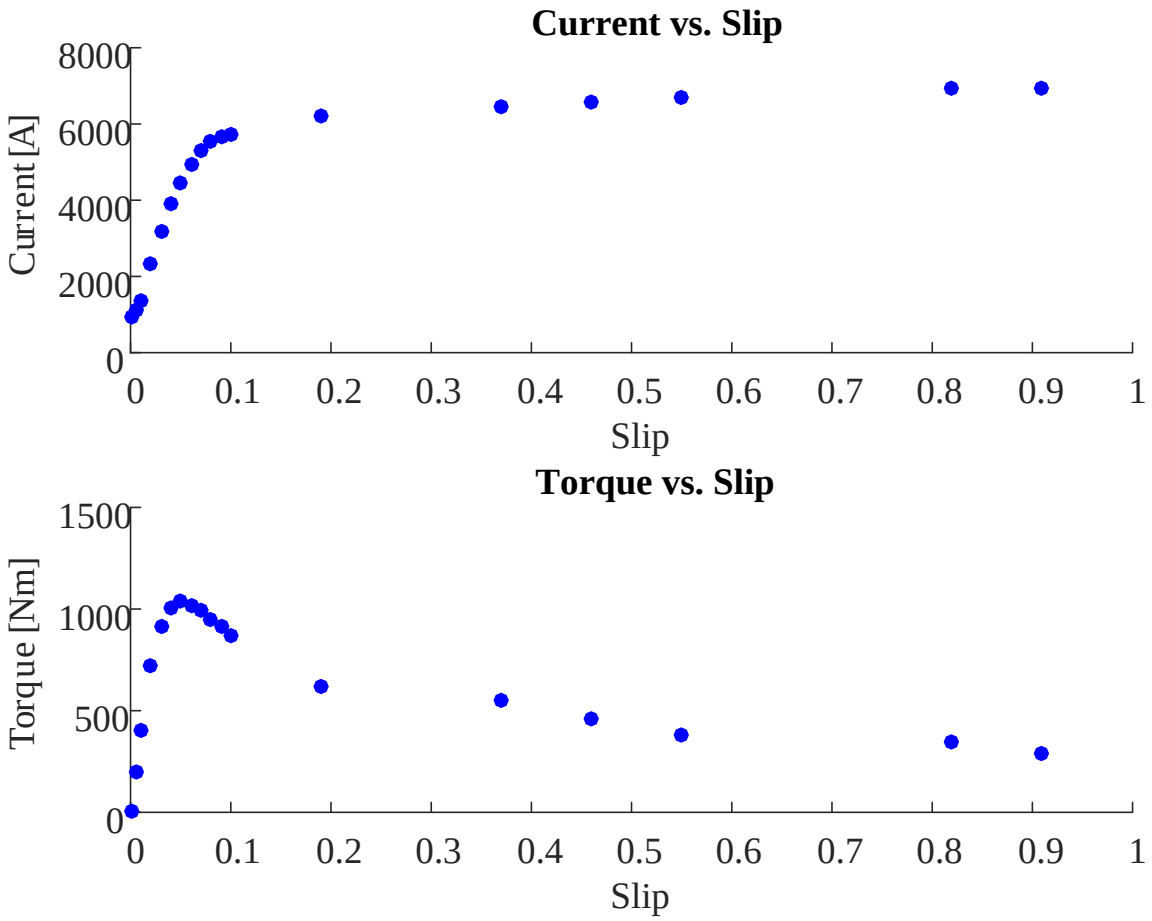

Figure 4.1: Results of the curve fitting algorithm on Current vs. Slip and Torque vs. Slip curves.

Table 4.1: Results of locked rotor and no load testing to be used as a baseline measurement for accuracy of proposed methods [10]

Rotor Resistance R_1	0.00867
Stator Resistance R_2	0.00325
Rotor Reactance X_1	0.00599
Stator Reactance X_2	0.009
Magnetizing Reactance X_m	0.15

More points are included in the low slip region intentionally, this is where the motor always operates, to the left of the breakdown point. Including more points in this region weights the useful portion of the curve more heavily in the curve fitting algorithm without any additional computations or the addition of a weighting factor.

In order to evaluate the effectiveness of the proposed algorithm error is considered and compared to the error of the alternative method. The alternative method for obtaining the equivalent circuit parameters makes use of results from locked rotor and no load testing. A summary of the equivalent circuit parameters from locked rotor and no-load testing is provided in Table 4.1.

Figure 4.2 shows the Torque vs. Slip and Current vs. Slip curves when the parameters found in locked rotor and no load simulations are used in the calculations compared to the simulation results seen in Figure 4.1.

The curves here clearly do not match well, with an average current error of over 50% and an average torque error of nearly 100%. A flaw in this method is that it is assumed that rotor leakage reactance and rotor resistance are constant and independent of slip.

The curve fitting algorithm proposed in this section is modified from [30] and generates equations for resistance and ractance which allow them to vary with slip.

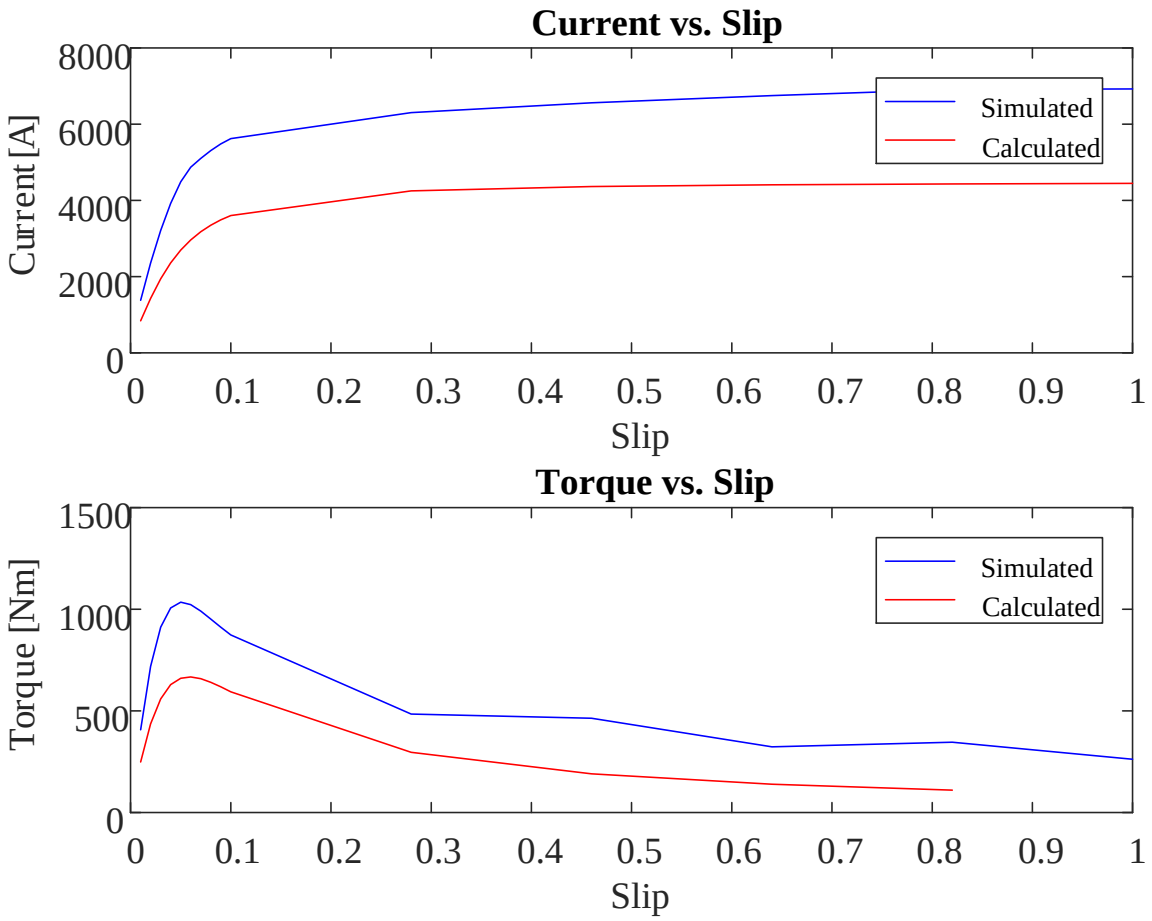

Figure 4.2: The simulation curves compared to calculated curves when the theoretical equivalent circuit parameters are used taken directly from locked rotor and no load simulations

It is applied here to the current and torque of the motor described in chapter 3. In the coming section the same algorithm will be applied to core and eddy current losses which will be used to calculate the overall efficiency at the end of the chapter.

The curve fitting generates R_2, and X_2 and magnetizing reactance X_m as polynomial functions of slip which can then be used to calculate output torque and winding current.

With mathematical relationships between slip and output Torque, current and

power the performance of the motor at all slip values can be calculated quickly and used in developing an efficiency map. The stator reactance and resistance can be assumed constant for the stranded winding motor and do not vary with slip. The remaining functions are shown in equations 4.1, 4.2 and 4.3.

$$R_2 = a + bs + cs^2 - ds^3 \tag{4.1}$$

$$X_2 = e + \frac{1}{fs - g} \tag{4.2}$$

$$X_m = h + \frac{1}{ms + n} + \frac{1}{s^2 + q} \tag{4.3}$$

The function of the optimization problem is to curve fit the measured Torque and Current values from a suitable number of simulations, with calculated values using the parameters above [30]. The optimization attempts to generate a vector of coefficients $x = [a, b, ..., q]$ which form polynomials for the rotor equivalent circuit parameters and estimate core losses.

The optimization problem makes use of the following multi-objective function, but could be modified to reduce the error in any two motor outputs that can be calculated from R_2, X_2, and X_m:

$$f_1 = w_1|I_{m1} - I_{c1}| + w_2|I_{m2} - I_{c2}| + ... + w_n|I_{mn} - I_{cn}| \tag{4.4}$$

$$f_2 = w_1|T_{m1} - T_{c1}| + w_2|T_{m2} - T_{c2}| + ... + w_n|T_{mn} - T_{cn}| \tag{4.5}$$

Here, the difference between the simulation torque or current at each point shown in figure 2.1 is compared to the results of calculating torque and current using the functions for R_2, X_2 and X_m above and the sum of those differences is the function

to minimize.

The weighting factors $w_1, w_2, ..., w_n$ are included to make the solution more robust. With these weighting factors an even distribution of points can be selected and the area to the left of the breakdown point made the focus of the optimization using weighting factors.

A multi-objective optimization problem such as this one will not give one optimal result. Rather, a pareto front of optimal results. The authors of [30] chose to study the best torque result and the best current result. However, this is not sufficient when extending the results to an application where only one set of equations can be used.

The pareto front in figure 4.3 shows that there are many points with low error in either the Torque domain or Current domain, however, when the two are considered together a balance must be struck. The selected point will have the lowest combined error in terms of percentage, therefore dividing the error in each domain by the average value in that domain and choosing the result with the lowest product of these fractions.

The results have too large error when considered over the entire operating range as shown, however, when considering only the points to the left of the breakdown point where the motor actually operates, the error is reasonable. Figure 4.4 shows these results.

The error in the low slip range (< 0.05) results are satisfactory (error is $< 4\%$). This is a large increase in accuracy compared to the locked rotor and no load testing parameter results shown in figure 4.2. These results could also be further improved by varying the parameters of the GA such as generations, population size and tolerance. The GA parameters used here are as shown.

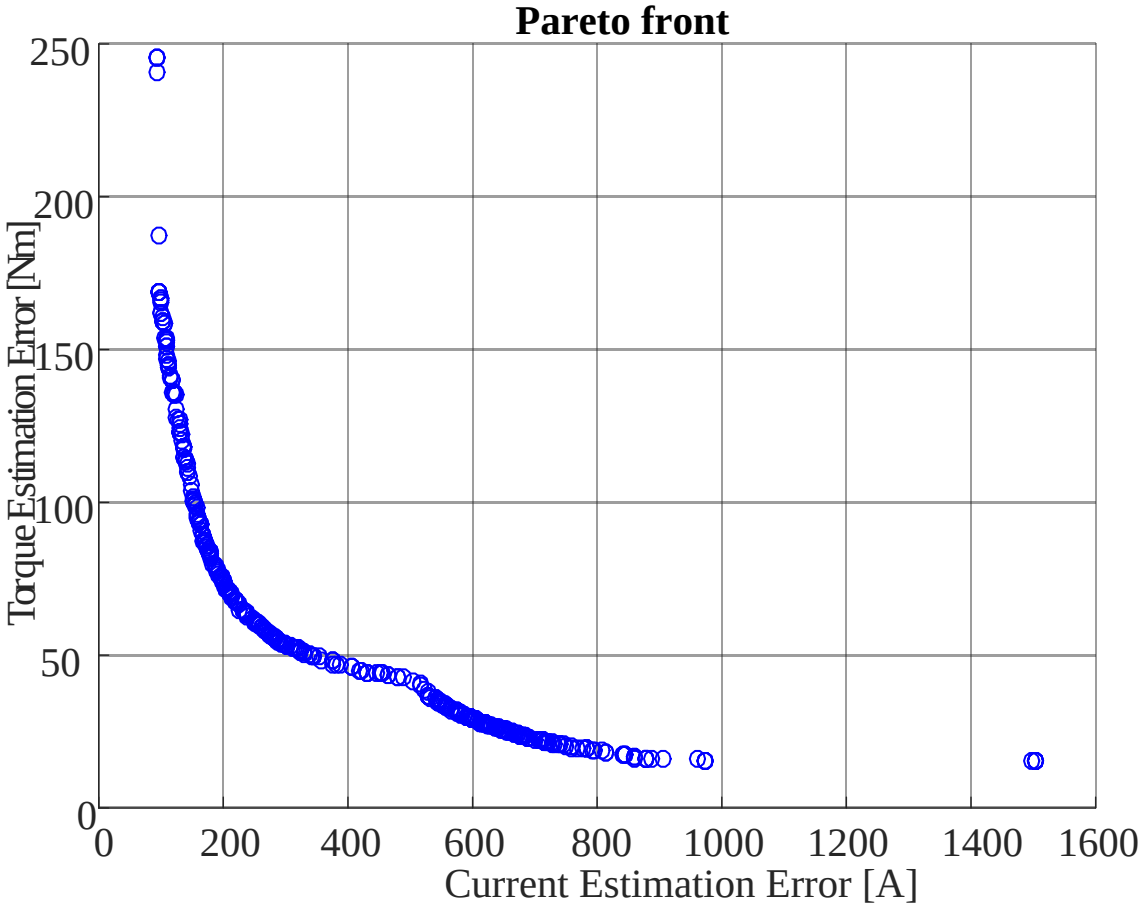

Figure 4.3: The Pareto Front for the multi-objective optimization function.

This method could be used to estimate torque and current for 160Hz at any slip. However, with voltage as an input the output Torque would vary with speed and core losses are always speed dependent. Another method which is independent of speed or accounts for speed in another way should be proposed. The GA parameters used in achieving the curve fits above are shown in table 4.2.

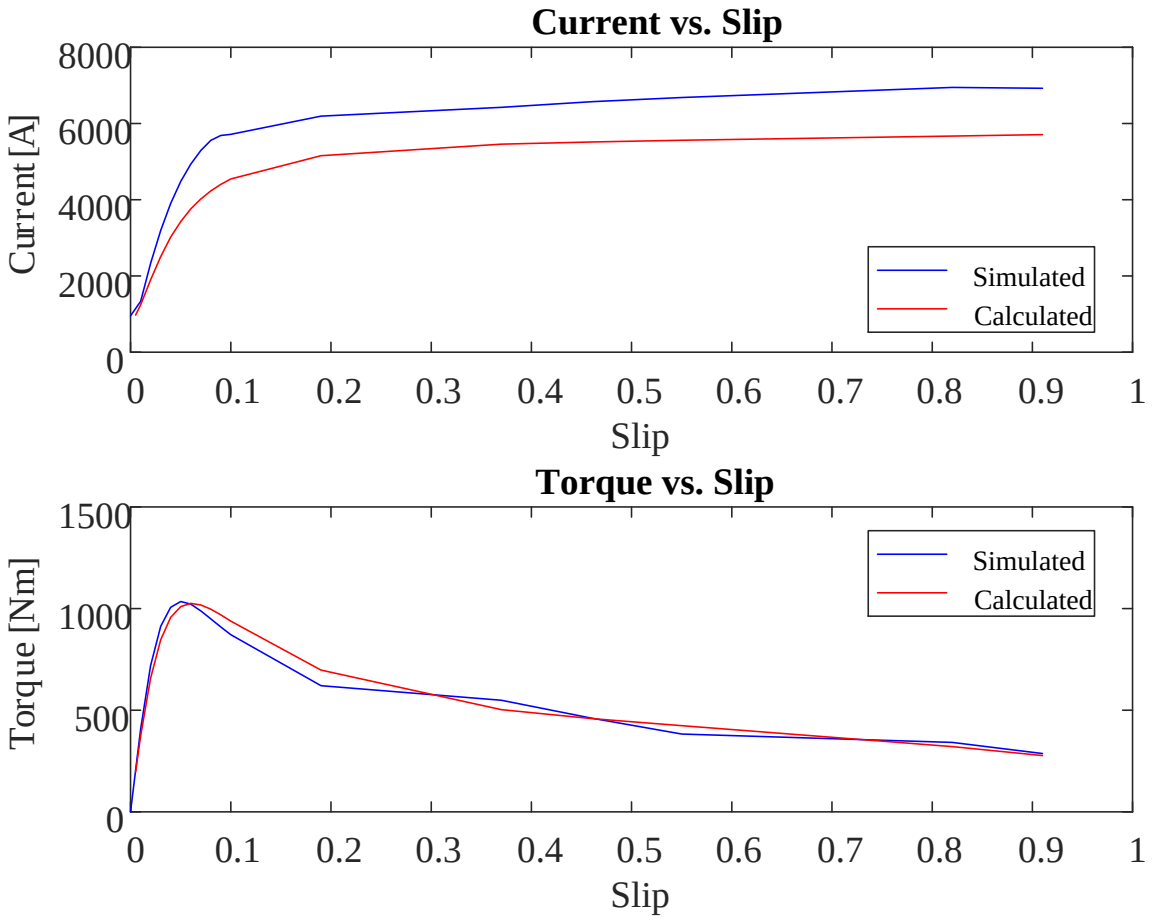

Figure 4.4: Results of the curve fitting algorithm on Current vs. Slip and Torque vs. Slip curves.

Table 4.2: Summary of genetic algorithm strategy parameters [10]

Population Size	2000
Number of Generations	1000
Number of Elite Individuals	10
Function Tolerance	0.003

4.2 Identifying Optimal Operating Points

One difficulty with benchmarking an induction machine is identifying optimal operating points. For each torque and speed combination that may be required by the driver, there are infinite voltage and slip combinations capable of reaching those performances. The methodology presented in the following section is capable of identifying the voltage and slip combination which minimizes the winding current and therefore losses.

Initially, as in the curve fitting section, voltage input was done in the sinusoidal form. To simplify analysis these will be converted first into a chosen dq reference frame where the q axis voltage is set to 0, and then into a second stationary reference frame where the q axis current is set to 0. The first transformation is done to simplify the simulation process and the output data, and the second transformation is done to simplify the optimal point selection algorithm to be used in creating the efficiency map.

$$\begin{aligned} &\text{Phase A} \quad V = Asin(2\pi ft) \\ &\text{Phase B} \quad V = Asin(2\pi ft - \frac{2\pi}{3}) \\ &\text{Phase C} \quad V = Asin(2\pi ft + \frac{2\pi}{3}) \end{aligned} \tag{4.6}$$

To work with the d and q axis coordinates the simulations must be set up such that either V_d, V_q, I_d or V_q are known. To achieve this voltage inputs are in the form:

$$\begin{aligned}
&\text{Phase A} \quad V = V_d cos(2\pi ft) + V_q sin(2\pi ft) \\
&\text{Phase B} \quad V = V_d cos(2\pi ft - \frac{2\pi}{3}) + V_q sin(2\pi ft - \frac{2\pi}{3}) \\
&\text{Phase C} \quad V = V_d cos(2\pi ft + \frac{2\pi}{3}) + V_q sin(2\pi ft + \frac{2\pi}{3})
\end{aligned} \tag{4.7}$$

And set $V_q = 0$ to minimize the number of unknowns. The output of the simulations will continue to express the winding current in phase A, B and C but the d-q axis currents can be easily calculated using equation 3.8.

$$I_d = \frac{2}{3}(-I_A cos(2\pi ft) - I_B cos(2\pi ft - \frac{2\pi}{3}) - I_C cos(2\pi ft + \frac{2\pi}{3})) \tag{4.8}$$

$$I_q = \frac{2}{3}(I_A sin(2\pi ft) - I_B sin(2\pi ft - \frac{2\pi}{3}) - I_C sin(2\pi ft + \frac{2\pi}{3})) \tag{4.9}$$

In the 3 phase system and equivalent circuit, voltage and current can be related via the expression:

$$\dot{V} = \dot{I} Z_{eq} \tag{4.10}$$

Where Z_{eq} is the combination of stator resistance and impedance in parallel with rotor resistance and impedance.

$$Z_{eq} = R_s + jX_s || jX_r + \frac{R_r}{s} \tag{4.11}$$

Now we wish to relate the d-q axis voltage to the d-q axis current.

$$\begin{bmatrix} V_d \\ V_q \end{bmatrix} = \begin{bmatrix} R_s + \frac{s\omega_{synch}^2 L_m^2 R_r}{R_r^2 + s\omega_{synch} L_r^2} & \frac{s\omega_{synch}^3 L_m^2 R_r}{R_r^2 + s\omega_{synch} L_r^2} - \omega_{synch} L_s \\ -\frac{s\omega_{synch}^3 L_m^2 R_r}{R_r^2 + s\omega_{synch} L_r^2} + \omega_{synch} L_s & R_s + \frac{s\omega_{synch}^2 L_m^2 R_r}{R_r^2 + s\omega_{synch} L_r^2} \end{bmatrix} \begin{bmatrix} i_d \\ i_q \end{bmatrix} \tag{4.12}$$

Or more simply:

$$\begin{bmatrix} V_d \\ V_q \end{bmatrix} = \begin{bmatrix} R & -X \\ X & R \end{bmatrix} \begin{bmatrix} i_d \\ i_q \end{bmatrix} \tag{4.13}$$

The stator resistance is a constant number and can be pulled out from this equation to simplify.

$$\begin{bmatrix} E_d \\ E_q \end{bmatrix} = \begin{bmatrix} V_d - R_s i_d \\ V_q - R_s i_d \end{bmatrix} - \omega_{synch} \begin{bmatrix} \frac{\omega_{slip} L_m^2 R_r}{R_r^2 + (\omega_{slip} L_r)^2} & -(L_s - \frac{\omega_{slip}^2 L_m^2 L_r}{R_r^2 + (\omega_s lip L_r)^2}) \\ L_s - \frac{\omega_{slip}^2 L_m^2 L_r}{R_r^2 + (\omega_s lip L_r)^2} & \frac{\omega_{slip} L_m^2 R_r}{R_r^2 + (\omega_{slip} L_r)^2} \end{bmatrix} \begin{bmatrix} i_d \\ i_q \end{bmatrix} \tag{4.14}$$

At this point synchronous speed/frequency is still part of the equation, so the results can only be applied to one frequency, a small line on the efficiency map. However, from the way it is expressed in 4.14 it is clear that ω_{synch} can be pulled out leaving a function of only slip frequency and current! This eliminates Voltage on the left side of the equation and leaves behind instead flux linkage (since $\frac{V_{ds}}{w_{synch}} = \Psi_{ds}$) so we can create an equation of the form:

$$\begin{bmatrix} \Psi_{ds} \\ \Psi_{qs} \end{bmatrix} = \begin{bmatrix} f_1(\omega_{slip}) & -f_2(\omega_{slip}) \\ f_2(\omega_{slip}) & f_1(\omega_{slip}) \end{bmatrix} \begin{bmatrix} i_d \\ i_q \end{bmatrix} \tag{4.15}$$

With f_1 and f_2 such that:

$$\begin{bmatrix} \Psi_{ds} \\ \Psi_{qs} \end{bmatrix} = \begin{bmatrix} \frac{\omega_{slip} L_m^2 R_r}{R_r^2 + (\omega_{slip} L_r)^2} & -L_s + \frac{\omega_{slip}^2 L_m^2 L_r}{R_r^2 + (\omega_{slip} L_r)^2} \\ L_s - \frac{\omega_{slip}^2 L_m^2 L_r}{R_r^2 + (\omega_{slip} L_r)^2} & \frac{\omega_{slip} L_m^2 R_r}{R_r^2 + (\omega_{slip} L_r)^2} \end{bmatrix} \begin{bmatrix} i_d \\ i_q \end{bmatrix} \tag{4.16}$$

It is now clear that it is possible to display flux linkages as functions of only i_{ds}, i_{qs} and ω_{slip} and the optimal point selection algorithm, in d-q coordinates is as follows. Note that the function to minimize is made up of output variables i_{qs} and i_{ds} which will not be evenly spread over the data. In order to work with the data in a way that can be grid fit to the input variables, either v_{ds} and v_{qs} must be known or set to zero, or either i_{ds} or i_{qs} equal to zero. This way, the optimization problem is only over two variables and a grid fit can be used for uneven spacing of the currents.

$$\begin{aligned} \underset{\omega_{slip}}{\text{minimize}} \quad & i_{ds}^2 + i_{qs}^2 \\ \text{subject to} \quad & T_e = \frac{3p}{2}(\psi_{ds} i_{qs} - \psi_{qs} i_{ds}) = T_{ref} \\ & u_{ds}^2 + u_{qs}^2 \leq (\frac{V_{dc}}{\sqrt{3}})^2 \\ & u_{ds} = R_s i_{ds} - \omega_{slip} \psi_{qs} \\ & u_{qs} = R_s i_{qs} - \omega_{slip} \psi_{ds} \\ & 0 \leq f(i_{ds}, i_{qs}) \leq I_{max} \end{aligned} \tag{4.17}$$

In the transition from equation 4.14 to 4.15, it is clear that in order to eliminate frequency or synchronous speed and make a model that works at all speeds, voltage must be replaced by flux linkage.

The simulations were run at 160Hz because this is the base speed of the motor. Therefore, this line lies in both the constant power and constant voltage region. Choosing a frequency higher than 160Hz would be ineffective since the high torque

levels are not reached. At lower frequencies, the trends seen in the constant power region may not be easily estimated. Therefore using only simulations run at 160Hz, over a variety of slip frequencies and input voltages, we are able to create a relationship between slip frequency, current and flux linkage which holds at all frequencies. However, currently there are two currents and two flux linkages at each point which makes the data cumbersome. Therefore, the solution must be to eliminate either i_{qs} or i_{ds} which will be done using the Park transformation.

The Park transformation converts from a two phase reference frame to a rotating frame. The first step is to define the new axes such that the existing d- and q- axis currents are maximized along the new d axis and 0 along the new q axis. The selected d' axis is shown in figure 4.5. The magnitude of I'_d is in equation 4.17 and the angle θ is calculated in equation 4.18.

$$I'_d = I = \sqrt{i_{ds}^2 + i_{qs}^2} \tag{4.18}$$

$$\theta = cos^{-1}(\frac{i_{ds}}{I'_d}) \tag{4.19}$$

Note that along the q axis currents sum to zero.

$$I'_q = -i_{ds}sin(90 - \theta) + i_{qs}cos(90 - \theta) \tag{4.20}$$

From there, the other variables can be projected to the new axes in the same way:

$$V'_{ds} = V_{ds}cos\theta \tag{4.21}$$

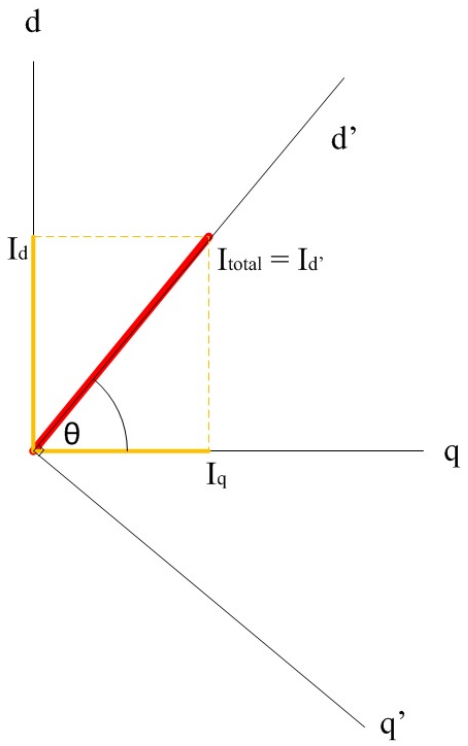

Figure 4.5: Figure showing how d' axis is selected from the projections of the original d- and q- axis currents

$$V'_{qs} = -V_{ds} sin\theta \tag{4.22}$$

$$\psi'_{ds} = \psi_{ds} cos\theta + \psi_{qs} sin\theta \tag{4.23}$$

$$\psi'_{ds} = \psi_{qs} cos\theta - \psi_{ds} sin\theta \tag{4.24}$$

And torque will be a calculation with only one current and one flux as shown:

$$T_e = 3/2 * pp * \psi'_{qs} I'_d \theta \tag{4.25}$$

A simple grid fit can also now be applied in MATLAB to make the uneven current data appear along usable grid points. Since the output will be a function of slip, d-axis current (also the total current due to the above changes) and q-axis flux, the q-axis flux as a contour of slip and current is shown.

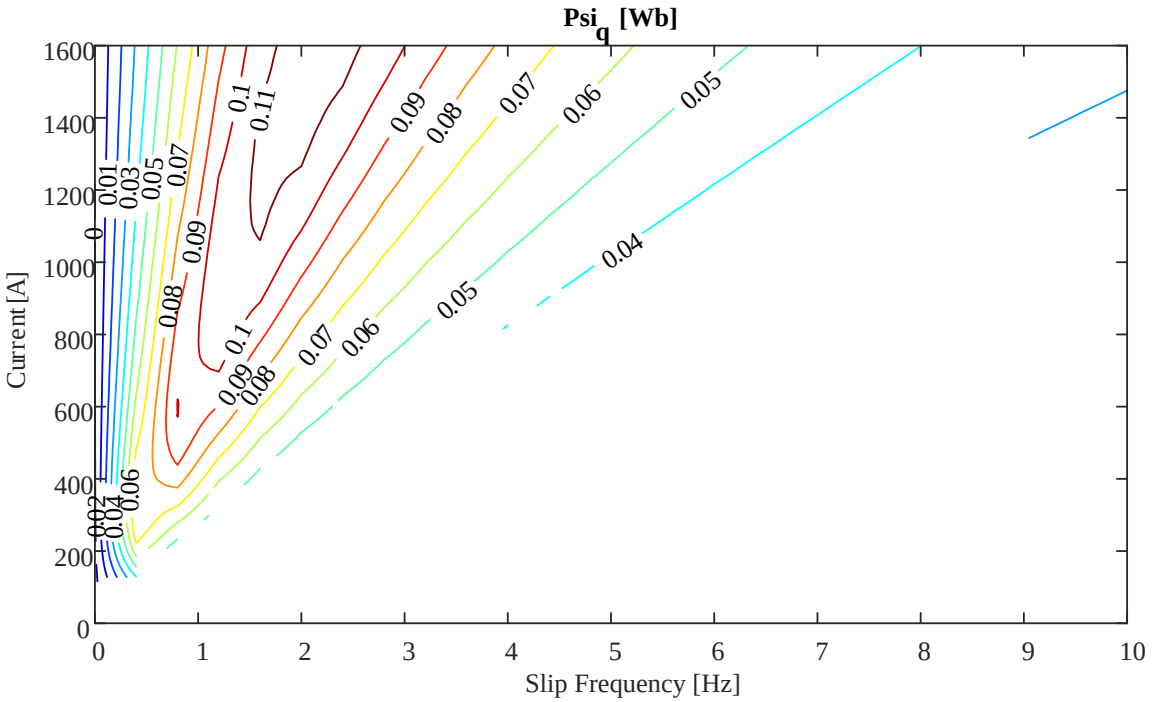

Figure 4.6: The grid fit Psi_q data created from 160 Hz results

With the number of variables reduced the minimization problem appears much simpler. Note that a similar contour plot to Figure 4.6 is created for d-axis flux as it is used in the optimization problem shown to limit the voltage.

$$\begin{aligned} \underset{\omega_{slip}}{\text{minimize}} \quad & I'_{ds} \\ \text{subject to} \quad & T_e = \frac{3p}{2}(-\psi'_{qs} I'_{ds}) = T_{ref} \\ & u_{ds}^2 + u_{qs}^2 \leq (\frac{V_{dc}}{\sqrt{3}})^2 \\ & u_{ds} = R_s I'_{ds} - \omega \psi_{qs} \\ & u_{qs} = \omega \psi_{ds} \\ & 0 \leq I'_{ds} \leq 900\sqrt{2} \end{aligned} \tag{4.26}$$

With the equations created and optimization process designed the following procedure was implemented in Matlab to create the efficiency map and loss map in the following section.

1. The maximum Torque that can be reached at each speed was found by running an optimization similar to above but with a different objective function

$$\begin{aligned} \underset{\omega_{slip}}{\text{minimize}} \quad & -T_e \\ \text{subject to} \quad & u_{ds}^2 + u_{qs}^2 \leq (\frac{V_{dc}}{\sqrt{3}})^2 \\ & u_{ds} = R_s I'_{ds} - \omega \psi_{qs} \\ & u_{qs} = \omega \psi_{ds} \\ & 0 \leq I'_{ds} \leq 900\sqrt{2} \end{aligned} \tag{4.27}$$

2. T_{ref} is varied from 10 to T_{max} found in step 1 for each speed and the optimization system described in equation 4.26 is applied iteratively at each speed and T_{ref}

3. Losses are calculated at each point - the measured losses at all points were grid fit as a function of I_d and Psi_q in the lookup table $Loss(160Hz)$ and normalized,

then curve fitting was applied over the speed range as done in section 4.1

To normalize the function $Loss(160Hz)$ a voltage to frequency ratio of 1 was selected. Therefore the point at 160V from the earlier simulations was selected where the core losses were measured at 961 Watts. Each value selected was then divided by this number.

$$Loss(160Hz)_{norm} = Loss(160Hz)/961 \tag{4.28}$$

The following polynomial was created using a curve fit algorithm similar to the one proposed in section 4.1. The coefficients to be curve fit a, b, and c can be seen in equation 4.29.

$$P_1 = aw_{rpm}^3 + bw_{rpm}^2 + cw_{rpm} \tag{4.29}$$

The results of the curve fitting is shown in Figure 4.7. Note that for this motor the copper losses in the stator are easily estimated so the curve fitting algorithm is a single objective function and does not make use of the pareto front. When a motor has more complicated stator winding losses, such as with unknown wire gauge or with bar windings the second objective will be to estimate stator winding losses.

Finally equations 4.28 and 4.29 are combined to calculate core losses.

$$Loss_{core} = P_1 Loss(160Hz)_{norm} \tag{4.30}$$

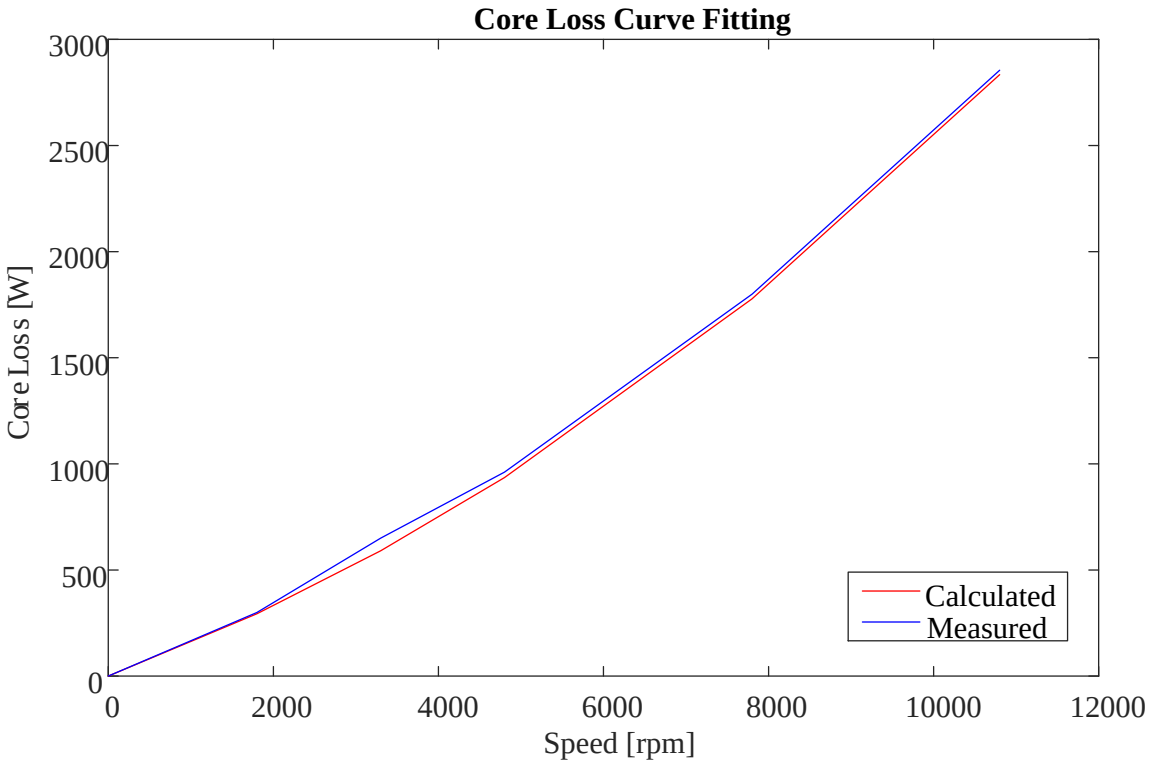

Figure 4.7: A curve fit for core losses ran at no load, V/f=0 over a number of frequencies

4.3 Motor Performance

The primary method for comparing motor performances that will be used in this study is the efficiency map.

The efficiency map for the representative motor described in Chapter 3, with the methodology described above can be seen in figure 4.8.

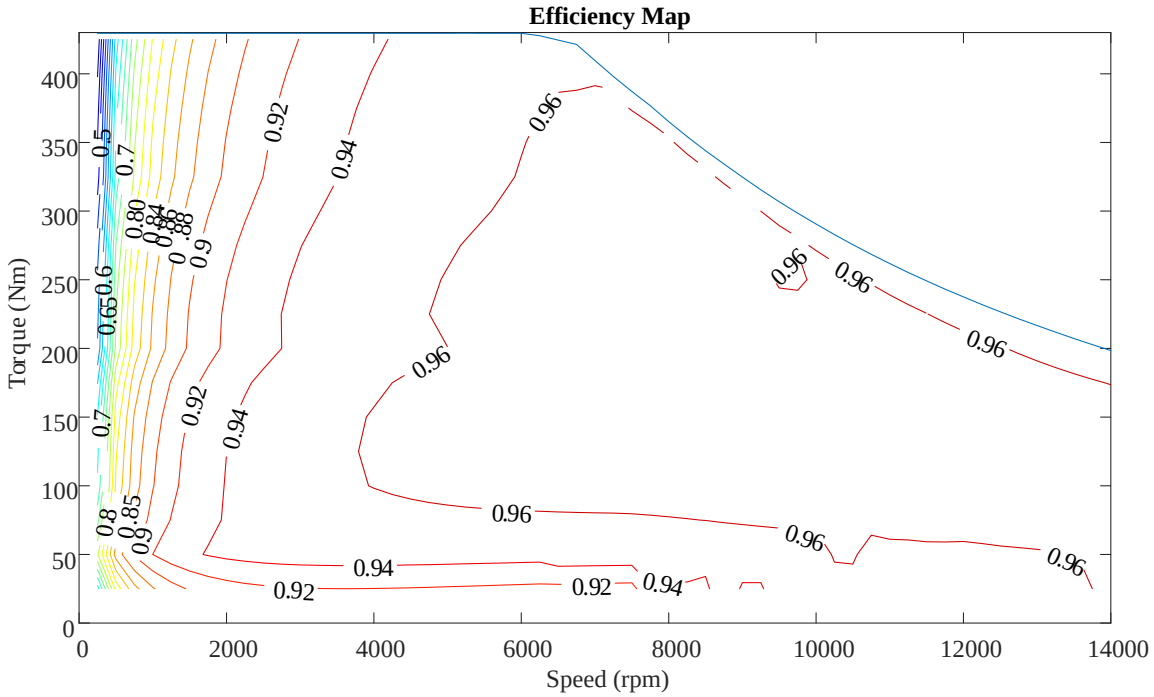

Figure 4.8: Efficiency map of the representative motor

4.4 Evaluating the Efficiency Map Creation Methodology

In order to validate the method for predicting efficiency that was proposed in sections 4.1 and 4.2 the efficiency was simulated at 4 priority operating points and compared to the efficiency map in figure 4.8. The losses are also compared directly in table 4.3.

Table 4.3: Comparison of the core losses found using the flux lookup tables and [10]

Operating Conditions	Simulated Value [W]	Calculated Value [W]	Error
T = 255Nm, w = 1050rpm	41.33	40.48	0.02
T = 200Nm, w = 3100rpm	297.18	282.73	0.04
T = 190Nm, w = 9000rpm	837.00	803.94	0.04

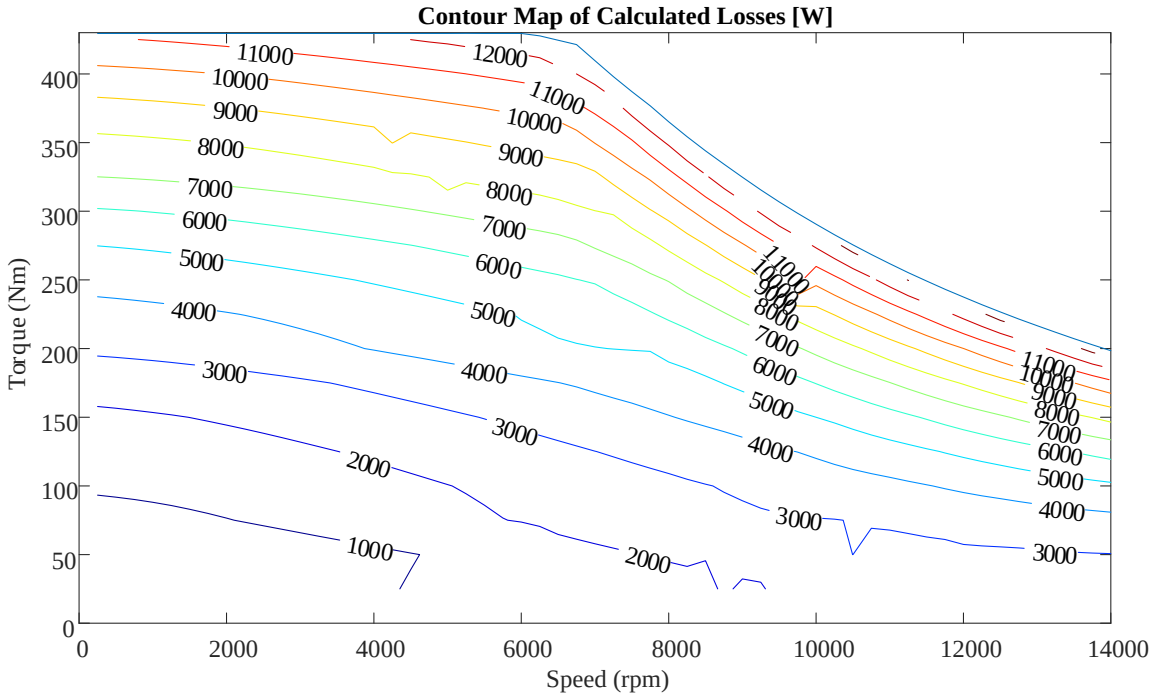

Figure 4.9: Loss contour plot for the representative motor

Finally, the efficiency map created is compared to one prepared in [9] for the simulated Tesla Motor. The motors have slight geometric differences and winding layout changes as the representative motor in this thesis was created from patents with parametrized lengths and geometry information from [10] . For example, immediately one can see that the motor in [9] has a slightly different slot depth of 19 mm rather than the 18.6 mm used in the representative motor. Additionally, the slightly lower efficiencies in figure 4.10 could result from the creators using a more traditional control scheme rather than the most efficient voltage and slip input for each desired torque and speed output.

The amount of simulation time saved by this method is abstract, as it depends on the coarseness of the various sweeps that have to be performed in the alternative case. At the very least a sweep of synchronous speed (excitation frequency) would be

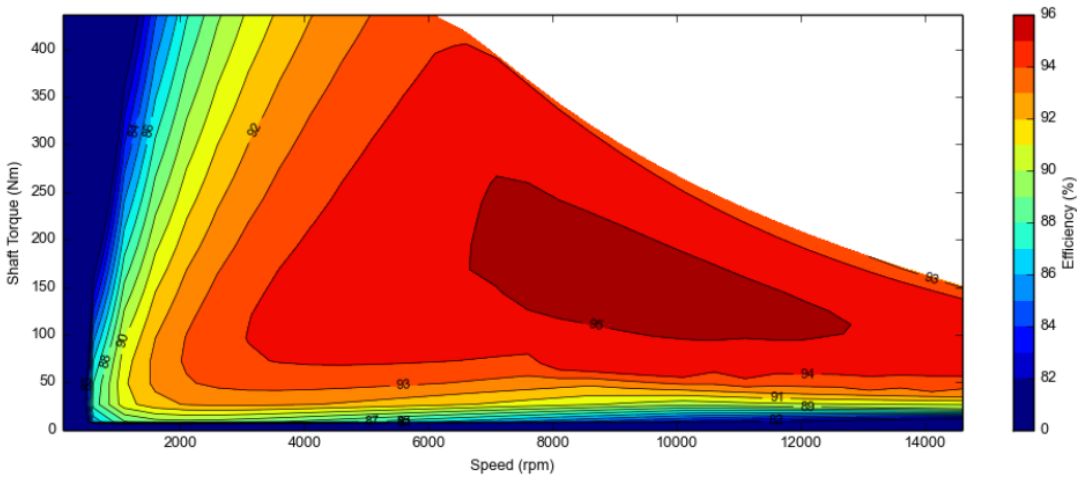

Figure 4.10: The efficiency map created in the study contucted for Motor Design Ltd. in [9]

required. Compared to a very coarse speed sweep of 1000 to 14000rpm at 1000rpm intervals, with varying currents and slips at these speeds, 1/14 of the simulations were required using the proposed methodology. A set of simulations was only done at 5000 rpm in this case. However, a finer sweep would be ideal and the number of simulations that would be required at each frequency to determine the optimal current and slip combination without mathematical minimization is difficult to estimate. Should it take only double the number of simulations to choose a slip/current combination through manually refining the points - the proposed methodology of this chapter requires only 1/28 of the total simulation time that would be required with an alternative method.

Chapter 5

Bar Windings In AC Induction Machines

Bar windings describe stator windings that are rectangular in shape. Rather than thin wires, these larger rectangles have a large cross-sectional area, chosen strategically, as well as a preset, systematic arrangement within the slots [11]. The cost of materials may be higher than their stranded counterparts, but manufacturing costs are lower and there is much less risk of wire damage during assembly. Coils and insulation take up the entire slot space, eliminating the random gaps between round wires. This eliminates coil movement and vibration during motor operation and therefore increases the durability of stator coils [11].

5.1 Improvements to Operation and Performance at Low and Moderate Speed Range

The advantages of bar windings stem from two major differences in their topology. First, there is a higher slot fill factor, and secondly, the shorter end turns with higher surface area.

These two results of bar windings lead to a number of differences in performance. In [13], the engineers responsible for changing the newer GM Chevrolet Volt and Bolt motors from a permanent magnet machine with stranded stator windings to stator bars summarize the major advantages as: improved torque per ampere, improved thermal performance, and improved high voltage protection. Stator bar windings are heavily studied in their applications in PMSM machines but there are limited studies on stator bars for IM.

5.1.1 Voltage Stress

The intentional layout of bars vs. random coils is most noticeable in machines with several turns. Consider a machine with four turns per slot. In order to have enough copper to relay the current, the stranded motor may have six strands in hand for each of these turns. This example will show, by comparison, a bar wound motor with one bar per turn.

In the coming sections the effect of position within the slot on eddy effects and flux will be discussed. Additionally, in a form wound motor, the turn-to-turn voltage stress will be uniform. This is because the induced voltage stress is greater between turn one and turn four, than it is between turn one and turn two. However, with

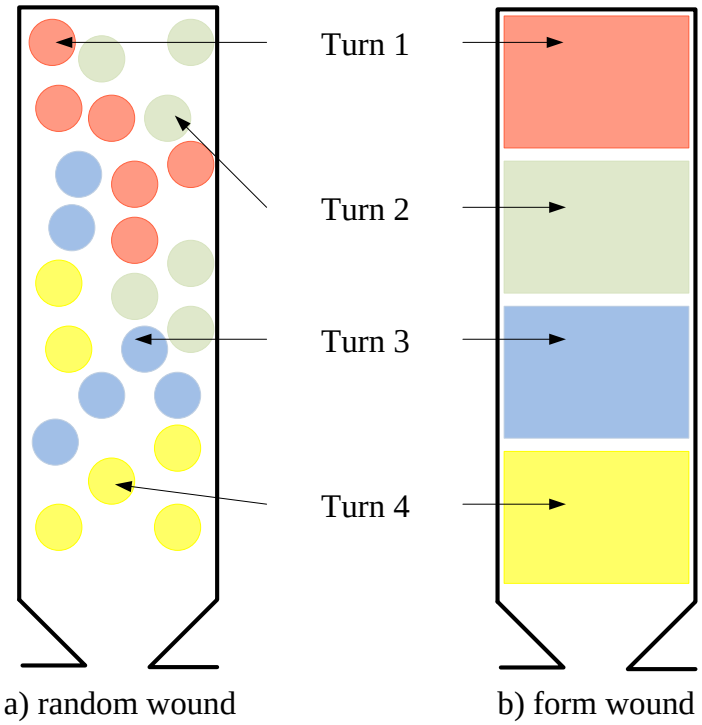

Figure 5.1: Random and form wound coils. The ability to keep an entire turn together and therefore a number of effects more uniform can be seen [11].

random windings it is impossible to ensure that a turn one coil will not end up next to a turn four coil. [11].

5.1.2 Current Density

Higher cross-sectional copper area means that the same applied current will have much lower current density and therefore lower DC resistive losses I^2R. The lower DC resistance and losses make for less heat dissipation and therefore better performance at transient conditions [5]. Lower resistive losses contribute to higher efficiency and higher peak torque when not limited by the inverter or current source. At speeds

up to 4000 rpm [15] notes a 0.2% — 5.2% increase in motor efficiency due to the lower resistive losses. By improving the slot fill and current density [15] claims a 40% reduction in DC resistance compared to an equivalent stranded design.

5.1.3 Thermal Performance

Thermal performance has a proportional relationship to losses — and therefore once again the improvements to thermal performance may be less prominent at high speeds where eddy effects are high [12]. In general, for speeds at which AC resistance is lower than DC resistance the thermal performance will be better. However, as a result of larger end-turn surface area, bar windings are much easier to cool. Therefore, the thermal performance may see additional improvements and may be better than the stranded design even at high speeds. For example, the Chevrolet Voltec motor designers in [15] claim a 20 degree Celsius lower temperature in a bar wound design versus a stranded design when an effective coolant is applied. The benefits are the ability to sustain peak torque for a longer period, higher efficiency, and lengthening of motor life. For the thermal analysis in [13], thermocouples were attached to several locations on the GM machine. The authors claim, as in [15], that their bar wound machine is able to maintain 60% of its peak torque continuously with their chosen coolant and a peak efficiency of 97%.

The FEA thermal analysis of another bar wound machine in [12] uses the stator winding losses as the source of heat. Using the thermal density λ, of the material and the losses at a variety of positions over the stator slot, the paper calculated temperature changes at a finite number of points using the equation:

$$-\nabla \bullet (\lambda \nabla T) = p_{loss} \tag{5.1}$$

The paper treats each bar separately and models the losses and temperature rise in each. The conclusion is that the temperature is highest near the slot opening and that the temperature rise can be mitigated using magnetic slot wedges. Overall, the authors maintain that stator bars will perform better than stranded windings in a thermal analysis.

5.2 Eddy Effects

The major disadvantage of bar windings comes in the form of eddy effects (skin and proximity) [13] [14] [15]. Eddy effects are defined as the difference between the total effective resistance losses and the DC resistance as calculated by I^2R. These eddy effects become increasingly apparent at high speeds as AC resistance increases. For example, the GM motor has a maximum speed of 9500 rpm, however, the designers note that it usually operates in the speed range below 4200 rpm and that the bar wound motor has better performance specifications at all speeds lower than 8000 rpm [13] [14] [15]. Until that point, the higher slot fill factor means that even with eddy effects, the effective resistance losses of the bar winding motor is lower. However, above 8000 rpm, the effective resistance exceeds that of the stranded winding design and the original motor is more efficient.

Eddy effects become increasingly apparent near the slot opening, as shown in figure 5.2.

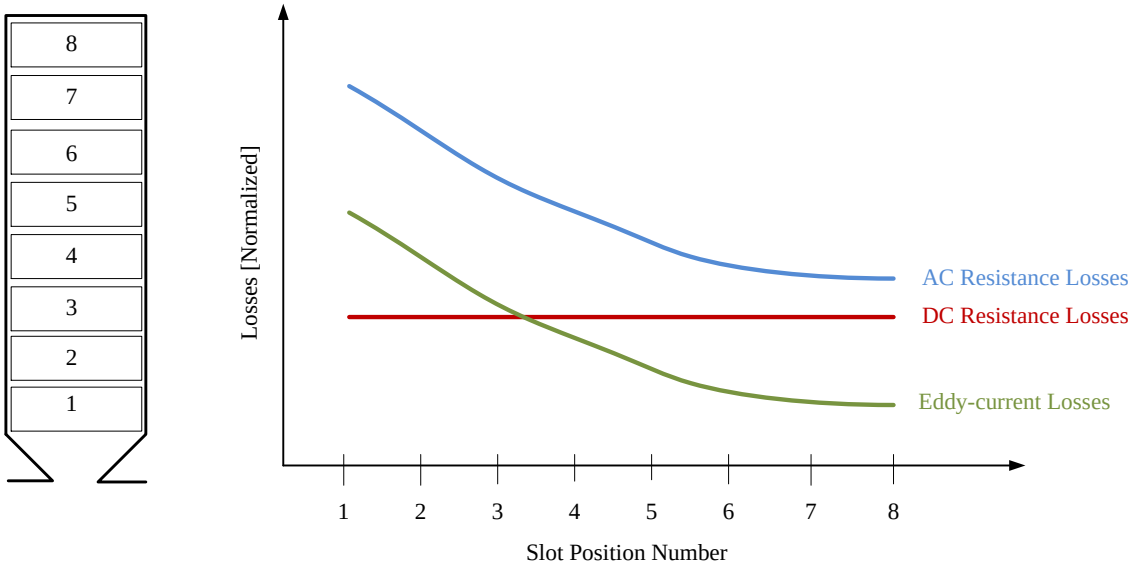

Figure 5.2: Both the AC resistance and eddy current losses are greater near the slot opening than toward the outside of the machine. The graph on the right is a unitless plot of losses at each of the slot positions shown in the diagram to the left. The units are removed to show the relationship more generally, but the figure is adapted from analysis performed in [12], where units do appear.

The shape of the slot opening has an influence on the eddy currents in the conductors, in addition to the position of the conductor in the slot. In [42] a motor is presented with form wound stator windings, in this case small flat copper conductors. In the paper, an open slot has less pronounced eddy currents in the conductors nearest the slot opening. This phenomenon is explained with flux leakage, which is higher in a semi-closed slot and emphasizes proximity effect near the airgap. Alternatively, the GM motor designers in [15] [14] use a very small slot opening, even placing it off-centre from the slot itself.

Designers often mitigate the effect of eddy currents by moving the stator bars further away from the slot opening (leaving some open space), optimizing the size of

the slot opening, or by introducing magnetic wedges in the slot opening.

Eddy effects are also more prominent at high speeds and at low currents as shown in figure 5.3.This is caused by the saturation of the material. When the material becomes saturated at higher current levels, the skin and proximity effects drop to that of the free space. In the image, we can see that the stranded resistance is better in the GM machine for operating speeds over about 4000 rpm. However, this number is theoretically expected to triple in a similar machine with 4 poles rather than 12.

5.2.1 Skin Effects

Skin effect is the phenomenon by which current flows on the outside surface of a wire or conducting bar. Skin depth is calculated using the conductivity σ, permeability μ, and excitation frequency in the equation:

$$\delta = \frac{1}{\sqrt{\pi \sigma \mu f}} \tag{5.2}$$

In an induction motor with both rotor and stator bars, eddy effects are doubly important to consider. The Representative motor discussed in Chapter 3 operates at speeds up to 14000 rpm, where eddy effects would be pronounced since copper losses in the stator winding have a correlation to the frequency of the motor current. In stranded windings the increased loss at high speeds is mitigated by choosing an appropriate wire gauge where wire radius is smaller than the skin depth. Eddy effects may still be present in these windings in the form of circulating currents but this will be less pronounced [43] It is ideal to have the AC resistance in the wires equal to the DC resistance. This can be achieved by using a wire radius smaller than the skin depth δ [42].

In figure 5.4, one can see the a theoretical contour plot for skin effect at low and high speeds. At a higher speed the skin depth becomes much smaller (note the red ring in the conductor to the right), and the current in the outer region is significantly higher. The area in the center of the conductor where the current is approaching zero is much larger.

The effective resistance, or AC resistance, a function of current and copper area, is therefore higher in the figure to the right where a higher current is flowing through a smaller area.

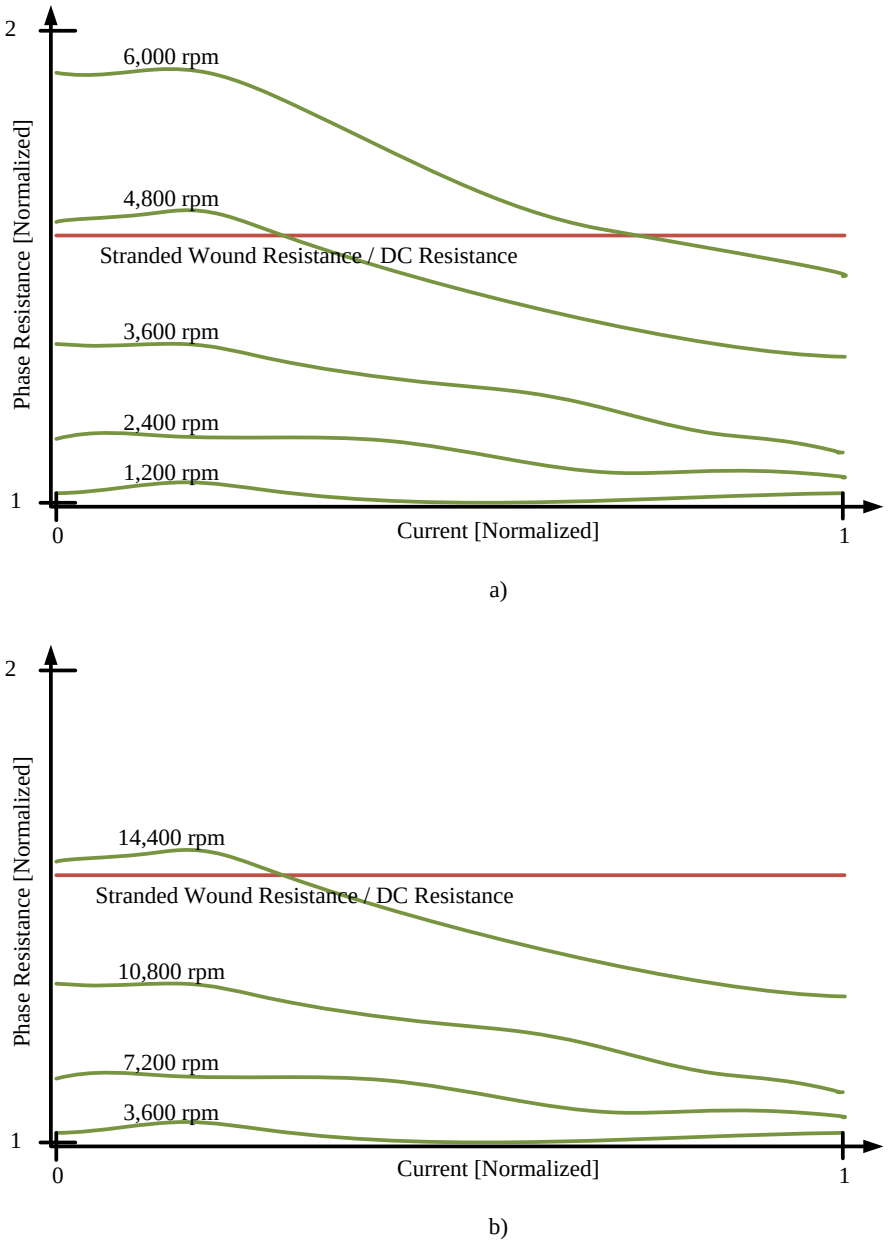

Figure 5.3: Here the AC resistance vs. current at a variety of speeds are shown in a normalized fasion for a) the 12 pole GM motor described in [13] [14] [15] ,and b) a comparable 4 pole motor.

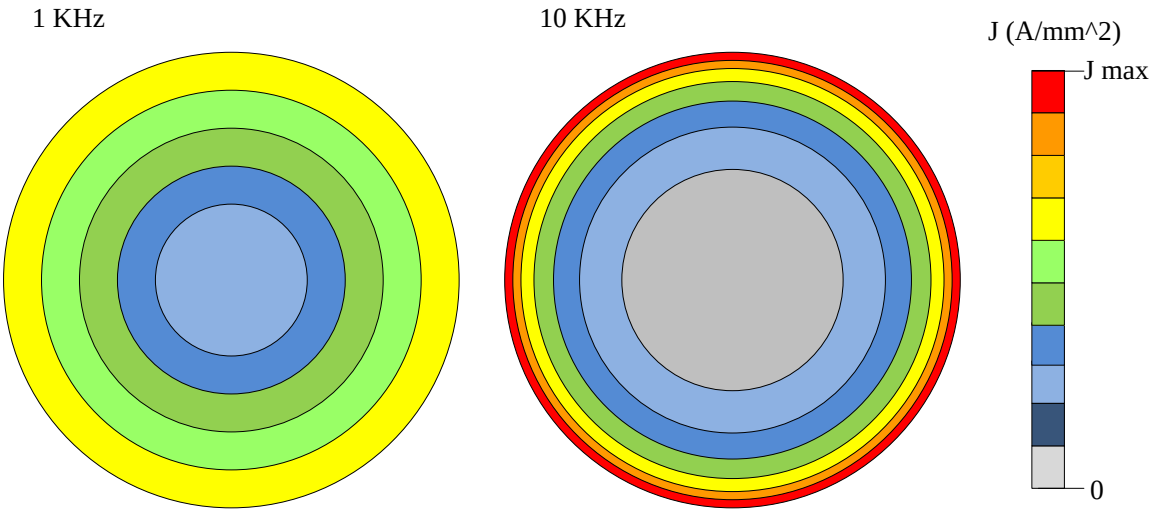

Figure 5.4: Skin effect as shown by the current density in two wires with the same applied current at low speed (1 kHz) and at high speed (10 kHz). Eddy effects are much more pronounced at high speed where the skin depth appears smaller and current density is very high at the perimeter of the wire [5].

5.2.2 Proximity Effects

Proximity effect differs from skin effect in that it is not the result of eddy currents from the conductor itself, but from the eddy effect of neighbouring conductors. Proximity effect occurs most in multilayer winding layouts at high speed operation [5]. Figure 5.5 shows the proximity effects in two scenarios: where the current is flowing in opposite directions in neighbouring wires, and where the current is flowing in the same direction.

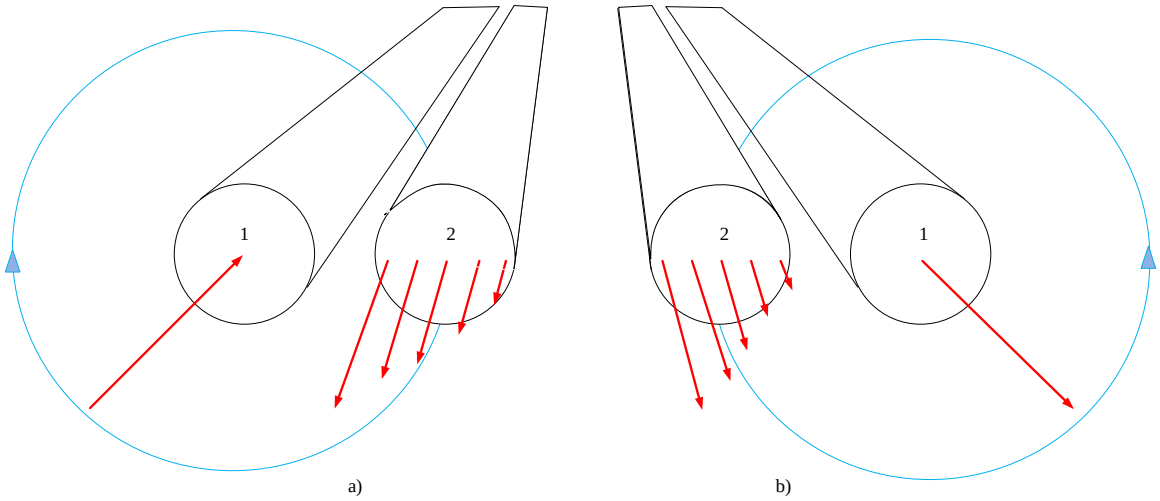

Figure 5.5: Proximity effect shown in wire 2 as caused by the magnetic field of conductor 1 for a) currents flowing in opposite directions, and b) currents flowing in the same direction [5].

In figure 5.5 b), where current flows in one direction, the proximity effects effectively cause skin effects as though the wires are all one conductor. Therefore, the highest current is on the outside of the group of conductors. Where the currents flow in opposite directions, the opposite appears to occur. However, if one considers the vector sum of the currents, it is clear that once again the most current flows towards the outside of the bundle of conductors.

For the machine in question, most slots contain two currents in phase flowing in the same direction, so the proximity effects will be most like those depicted in 5.5 b).

5.3 Estimating Copper Losses with FEA and Equivalent Circuit Models

The equivalent circuit presented in section 2.5 makes use of a simple resistor and inductor for stator losses, which can easily be included in an analysis with resistance, inductance, and current alone. In [44], a new equivalent circuit is presented which includes the eddy effects of both the rotor and stator. Since the stator losses in this thesis are being estimated using $P_{Rcu} + P_{Rfe} = (1 - slip)P_{ag}$, the equivalent circuit in figure 5.6 uses the ideas presented by [44], and applies them only to the stator winding of the equivalent circuit.

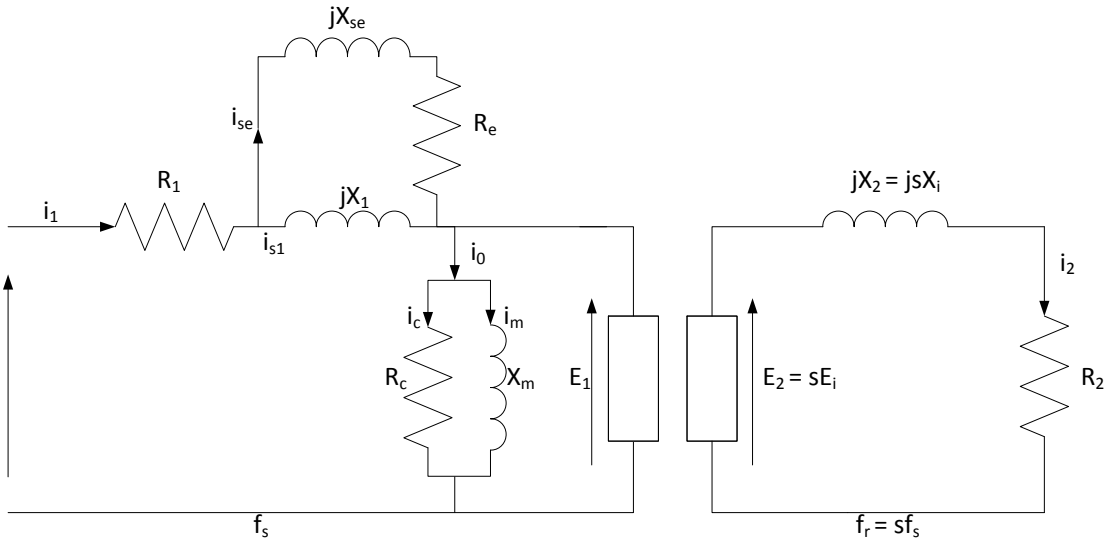

Figure 5.6: The induction motor equivalent circuit from chapter 2 altered to include AC inductance and resistance variables.

The paper's methodology begins with calculating eddy effect as the total resistive losses minus DC resistance losses as in [12].

$$P_{eddy} = P_t - \sum_{j=1}^{m} R_{dc} i_j^2 \tag{5.3}$$

In [44], the additional work of estimating P_{eddy} and the other power capabilities of the machine is done by analysing the equivalent circuit proposed, which is similar to the circuit shown above. Following their logic with the circuit in figure 5.5, the equation for torque is derived in the following steps:

The impedance for the stator coils is therefore no longer simply $R_s + sX_s$ where s is slip, but:

$$Z_s = R_s + (\frac{1}{sX_s} + \frac{1}{sX_s}) \tag{5.4}$$

and stator flux can be calculated with equation 5.5:

$$\psi_s^* = X_s i_s + X_{se} i_{se} + X_m(i_{s1} + i_{se} + i_2) \tag{5.5}$$

The torque calculation then changes to include this newly calculated flux. In d-q terms this appears as:

$$T_{eq} = \frac{3}{2} pp((\psi_s^*)_d (i_s)_q - (\psi_s^*)_q (i_s)_d) \tag{5.6}$$

This circuit is verified by estimating the circuit parameters for a number of different cases and comparing the results of time-discretized FEA to the results of the circuit in [44].

Chapter 6

Induction Motor with Bar Windings for Electric Propulsion Applications

6.1 Motor Topology

Dimensions for a motor with bar windings for comparative analysis is presented in this chapter. The goal in this motor design is to create a direct comparison between stator and bar windings, allowing for the advantages and disadvantages of each to be highlighted. In order to produce a fair comparison the geometry is mostly unchanged from the geometry presented in chapter 3. Most importantly, the slot area must remain identical so that the change in copper surface area can be attributed entirely to the increased slot fill factor rather than to geometry changes. However, to create a realistic bar wound motor the slot shape must be changed slightly. The main idea of bar windings is to increase the slot fill area and allow for easy manufacturing, to

achieve both of these objectives with a rectangular bar coil it is logical to have rectangular slots which accommodate two identical rectangular bars leaving just enough space for the insulation.

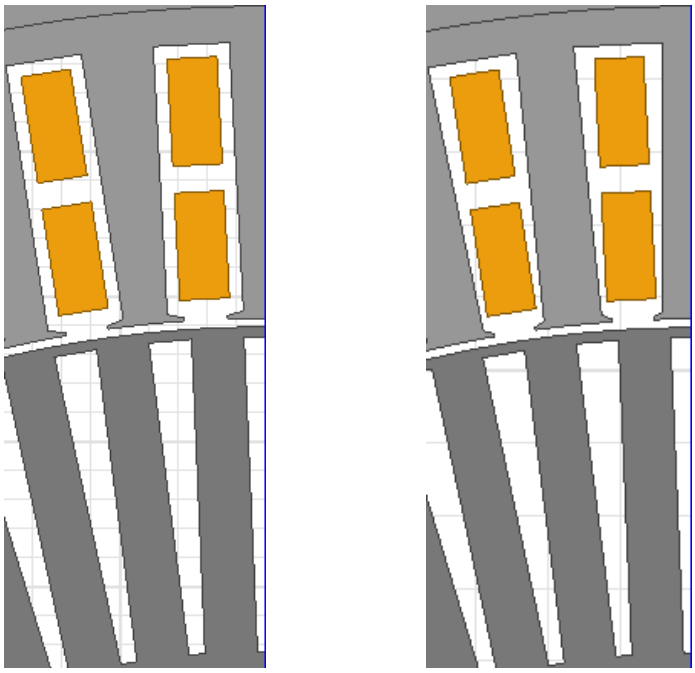

Figure 6.1: a) shows the parallel slot used for the bar winding model and b) shows the parallel teeth used in the representative Tesla motor with stranded windings. The change to parallel slots is made so that rectangular bar windings have the highest slot fill factor and are well suited to the shape of the slot

In figure 6.1 b) the inner coil cannot maintain a rectangular shape and get any wider because the edge closest to the air gap is approaching the stator tooth. By leaving the slot area the same but switching to a rectangular slot in a), one can see that both coils (unchanged) have room to be made wider in the final design and still accommodate a slot liner or insulation.

The final area of copper per layer in the parallel slot design is $29.49mm^2$ vs.

$25.29mm^2$ for copper bars with parallel teeth and $23.82mm^2$ of copper in the stranded winding motor. The slot fill factors of the stranded wound motor is therefore 48% and the slot fill factor in the bar wound motor is 61%.

6.2 Required Changes in Methodology due to Bar Windings

The procedure described in section 4.2, and mathematics described in equations 4.27 to 4.29 was applied again to the bar wound motor. However, the loss calculations (step 3) were somewhat altered. The grid fit, normalizing and curve fitting was applied to both the measured core losses and the measured eddy current losses in the stator windings. In this case, when validating the efficiency map results both the eddy losses and core losses, or simply the total losses, should be validated.

The copper loss curve also fit better with a fourth order polynomial than a cubic one and was much more sensitive to small changes in the coefficients - even the removal of significant digits.

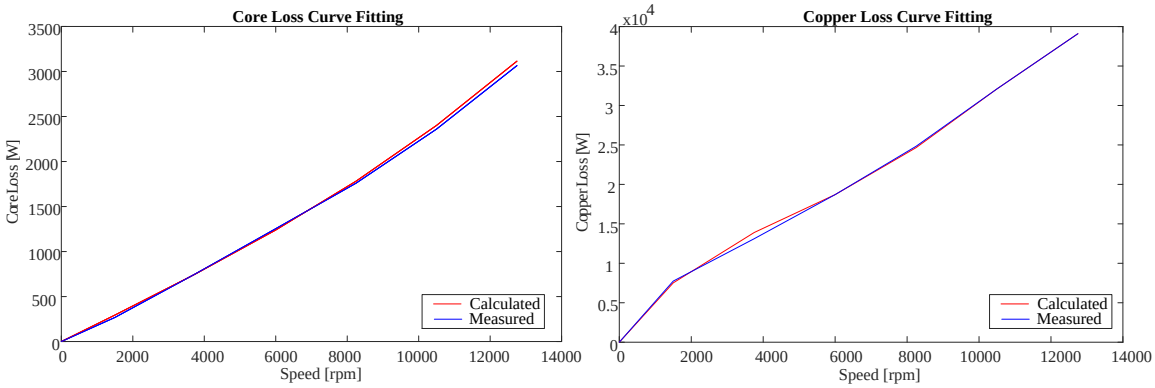

Figure 6.2: Results of a fmincon curve fitting algorithm on the core and copper losses for the bar wound machine

The optimization algorithm done for each point was slightly more computationally expensive for this motor because two grid searches, interpolations and curve fits were required for each loss calculation rather than one. For the stranded winding motor, stator copper losses had been estimated using resistance ie. based on the equivalent circuit.

The torque speed curve was generated with the minimization problem in equation 6.1 and the efficiency map with 6.2.

$$\begin{aligned} \underset{\omega_{slip}}{\text{minimize}} \quad & -T_e \\ \text{subject to} \quad & u_{ds}^2 + u_{qs}^2 \leq (\frac{V_{dc}}{\sqrt{3}})^2 \\ & u_{ds} = R_s I'_{ds} - \omega \psi_{qs} \\ & u_{qs} = \omega \psi_{ds} \\ & 0 \leq I'_{ds} \leq 900\sqrt{2} \end{aligned} \tag{6.1}$$

$$\begin{aligned} \underset{\omega_{slip}}{\text{minimize}} \quad & I'_{ds} \\ \text{subject to} \quad & T_e = \frac{3p}{2}(-\psi'_{qs} I'_{ds}) = T_{ref} \\ & u_{ds}^2 + u_{qs}^2 \leq (\frac{V_{dc}}{\sqrt{3}})^2 \\ & u_{ds} = R_s I'_{ds} - \omega \psi_{qs} \\ & u_{qs} = \omega \psi_{ds} \\ & 0 \leq I'_{ds} \leq 900\sqrt{2} \end{aligned} \tag{6.2}$$

6.3 Motor Performance

The major difference in the efficiency of the two motors will come from stator losses. The increased slot fill factor will lower stator losses at low speeds, but eddy effects have the potential to raise them significantly at high speeds.

Figure 6.3 shows the simulation results for the motor at 10000 rpm, where eddy effects are expected to be pronounced. The simulation captures the higher current flow toward the slot opening, a combination of skin and eddy effects. The eddy effects appear to be more pronounced in the conductor closer to the slot opening. If the conductors were in parallel, we might expect to see almost no current in the further conductor and higher current density at the slot opening. However, the conductors in this case are in series and therefore the total current flowing through each will be equal.

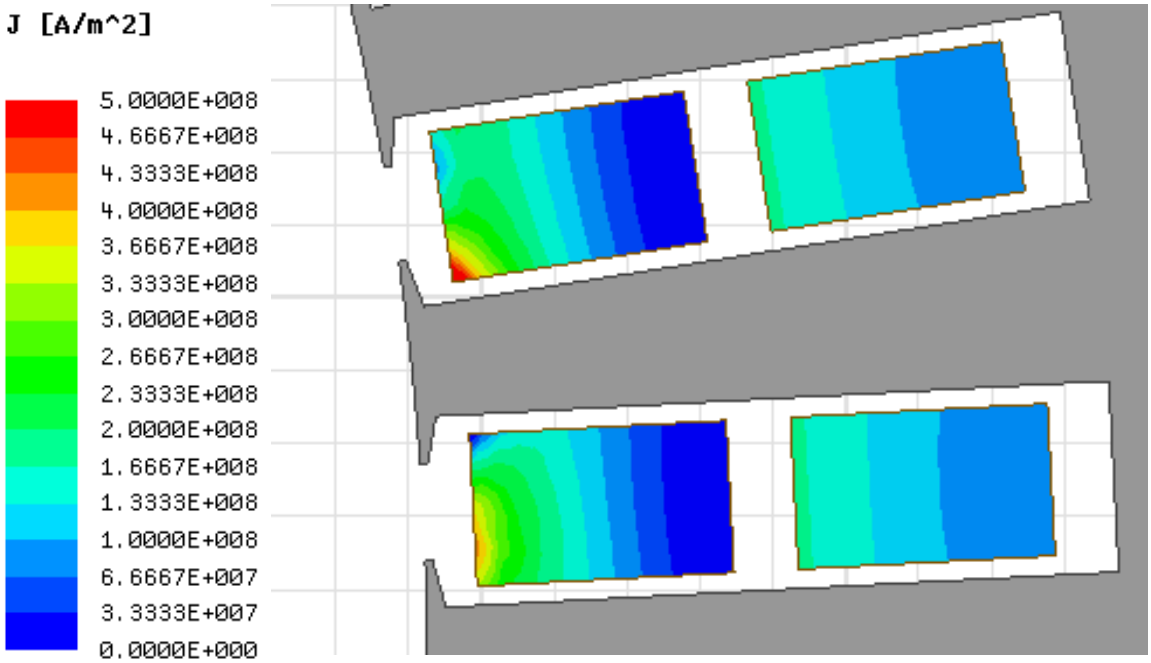

Figure 6.3: Current density in the bar windings in 2 slots at 10000 rpm

The efficiency map for the bar wound motor can be seen in figure 6.4 and the corresponding loss contour plot is shown in figure 6.5. Since the losses increase largely in the same pattern as power it creates a large section of the efficiency map where the efficiency is constant. One can see the centre portion across almost the entire torque range and up to a speed of 12000 rpm in some places, the efficiency is 89%.

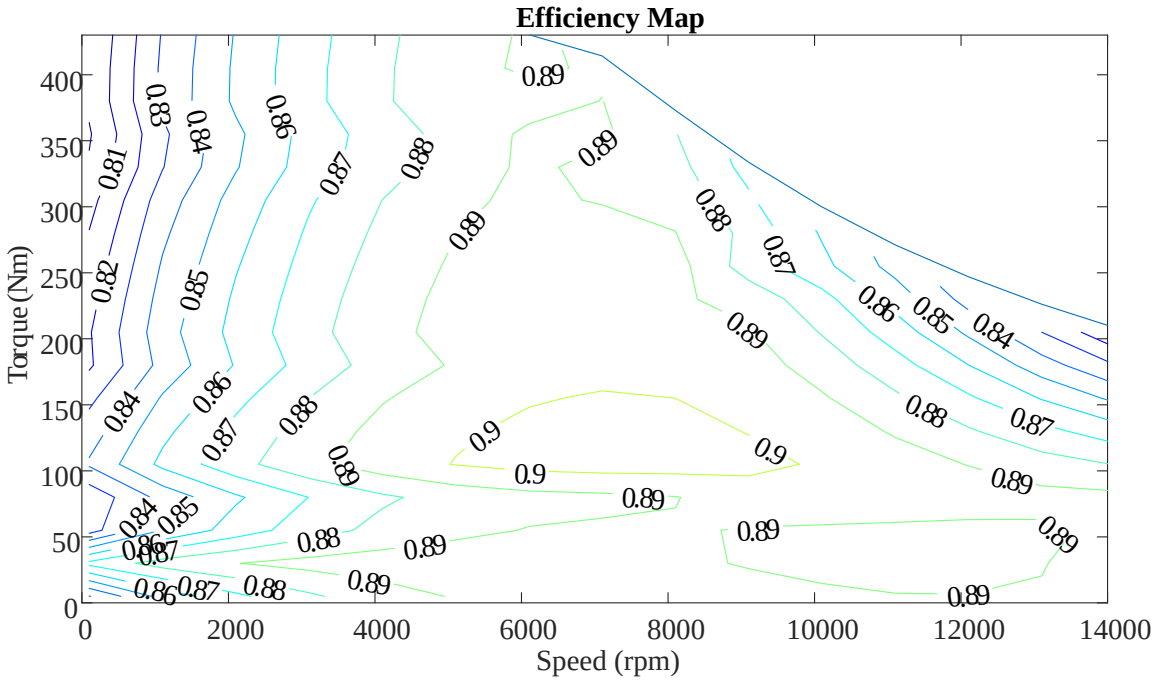

Figure 6.4: Efficiency map for the bar wound motor

6.3.1 Validating Results

The calculated loss results are confirmed with simulations as was done in chapter 4. Table 6.1 and 6.2 summarize the difference between the calculated and simulated results of core losses and stator copper losses, respectively. The points were selected

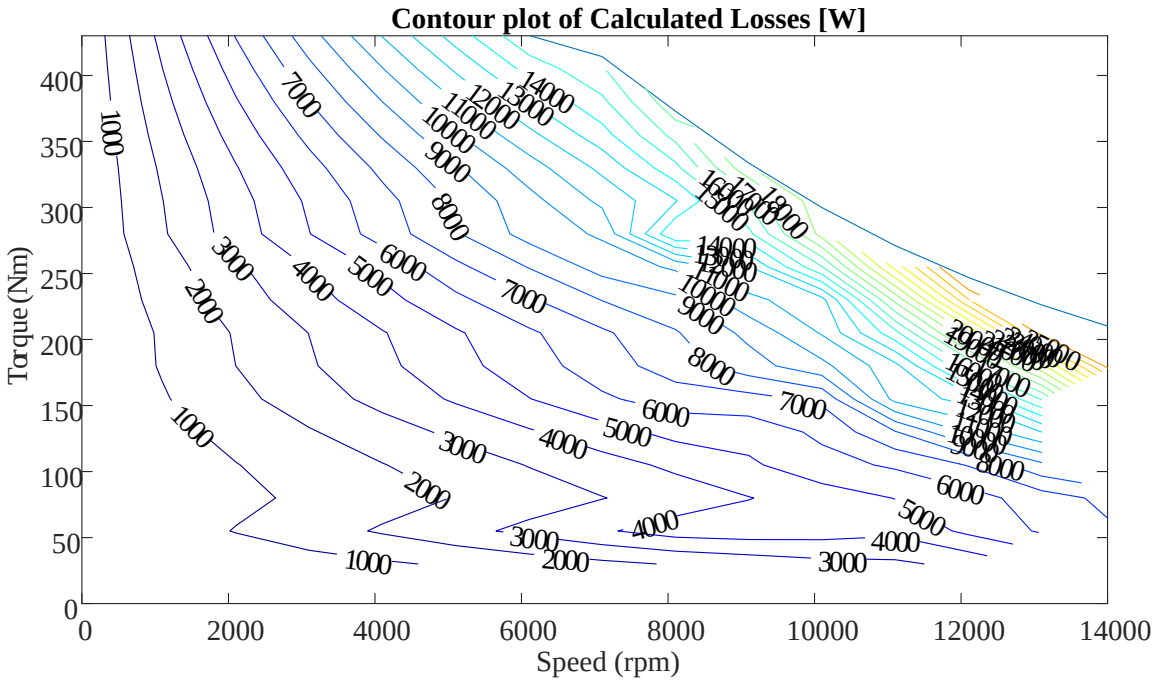

Figure 6.5: Contour plot of losses for the bar wound motor inside the torque speed curve

outside of the 5000 rpm data set as the accuracy would be highest here, since calculated results are simply interpolated from the simulation results at this speed, and skew the evaluation of the methodology. The efficiency values calculated with the losses in tables 6.1 and 6.2 have an error of under 0.003 for the three points.

Table 6.1: Comparison of the core losses found using the flux lookup tables and [10]

Operating Conditions	Simulated Value [W]	Calculated Value [W]	Error
T = 120Nm, w = 576rpm	124	130	0.05
T = 175Nm, w = 11900rpm	900	867	0.04
T = 190Nm, w = 5200rpm	319	306	0.04

Table 6.2: Comparison of the eddy current losses found using the flux lookup tables and [10]

Operating Conditions	Simulated Value [W]	Calculated Value [W]	Error
T = 120Nm, w = 576rpm	2550	2523	0.01
T = 175Nm, w = 11900rpm	7800	7520	0.04
T = 190Nm, w = 5200rpm	3213	3062	0.05

6.4 Comparative Analysis

Before comparing the results of the efficiency map creation algorithm, the basic torque vs. slip curves at base speeds are compared. Figure 6.6 compared the torque vs. slip curves and current vs. slip curves of both motors at base speed.

$$\tau_{max} = \frac{3V_1^2}{2\omega_{sync}(R_1 + \sqrt{R_1^2 + (X_1 + X_2)^2})} \tag{6.3}$$

Studying the equation above [16] one can see some variables which have changed with the new layout and some which have not. Input voltage and synchronous speed will remain unchanged. The difference in peak torque therefore depends on the change in stator resistance and reactance. With the increase in copper area it is reasonable that the resistance may be lower in the bar wound motor, and maximum torque therefore higher. However, due to the relative size of the X_1 and R_1 terms it is more likely that the higher torque is related to leakage inductance.

$$s_{max} = \frac{R_2}{\sqrt{R_1^2 + (X_1 + X_2)^2}} \tag{6.4}$$

It appears that the bar wound motor does not reach its maximum torque or breakdown slip under a slip frequency of 10 Hz. Figure 6.7 shows the Torque vs. Slip

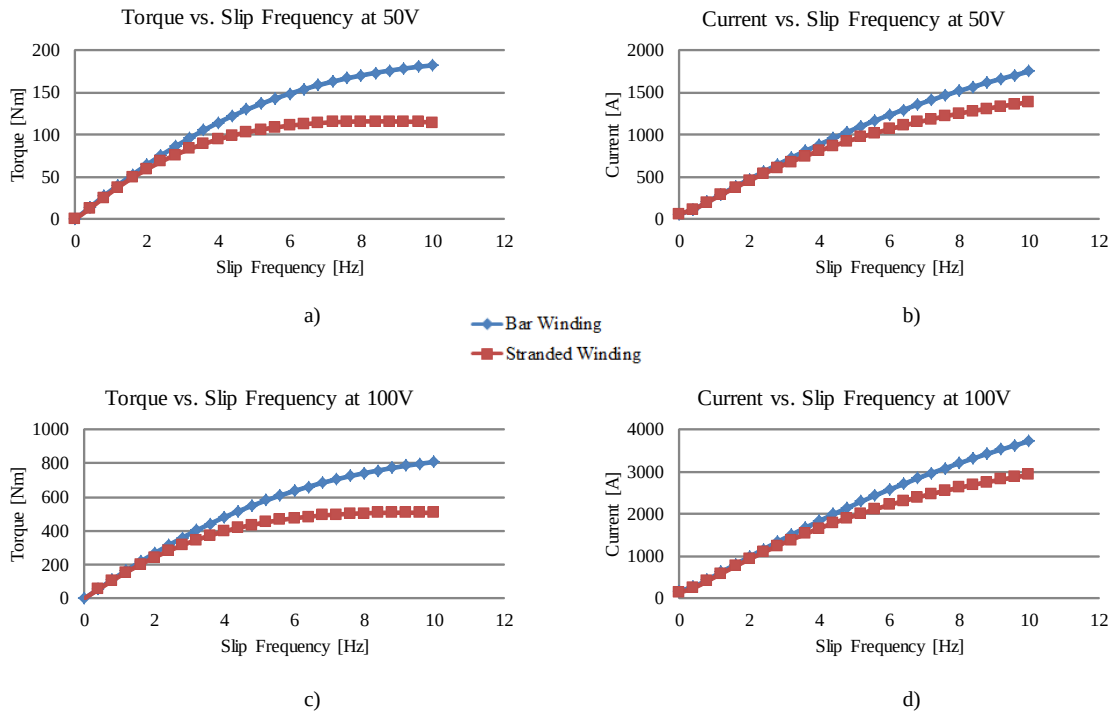

Figure 6.6: Torque vs. Slip and Current vs. Slip curves for the bar wound and stranded wound motor at 50V (a) and b)) and 100V (c) and d)) input current at 160Hz

curves up to a higher slip frequency of 18 Hz.

In this study the current was limited by the inverter, however, in chapter 6 it was discussed that the thermal and resistive losses of the GM motor with bar windings would allow the motor to maintain 60% of its peak torque continuously if given an adequate current supply. For the 100V example, which is not the maximum voltage of the machine, this would correspond to a torque of 530Nm based on the peak torque in figure 6.7. With the notably higher peak torque seen in figure 6.7 the continuous or rated torque of the machine would also be significantly increased. The thermal losses may not be the same for the motor designed. Section 6.4.2 will expand on the stator winding losses and, one factor contributing to the thermal performance.

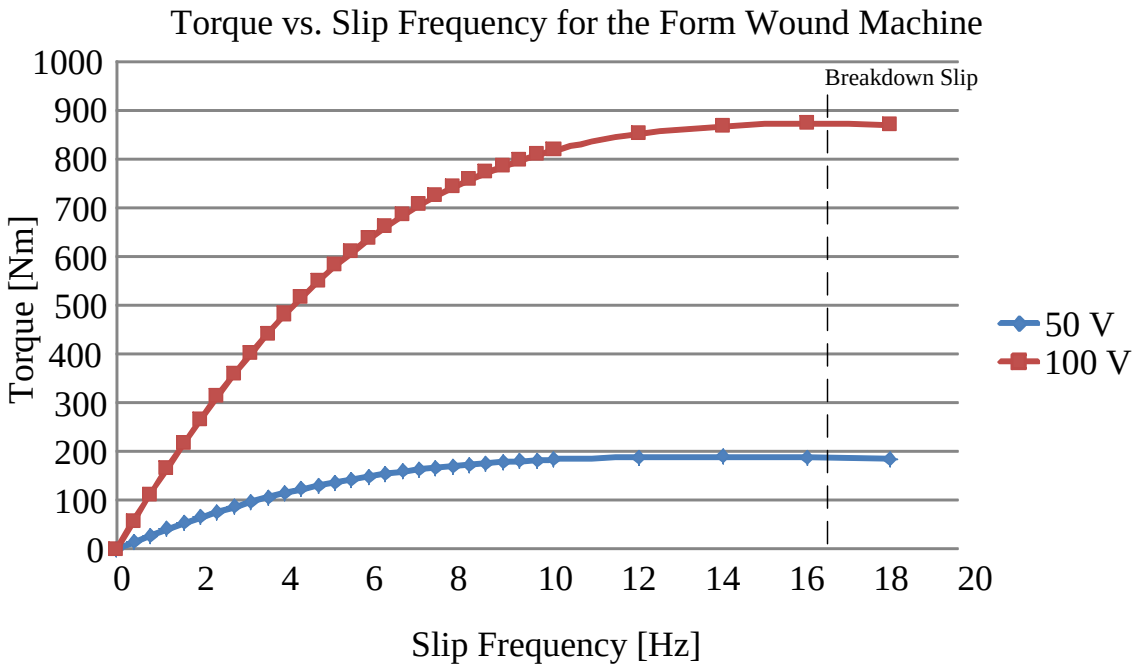

Figure 6.7: Torque speed curve for the bar wound motor at base speed for two different voltages

6.4.1 Losses and Efficiency

The major differences in the losses are expected to be in the eddy current losses. To confirm this, it is interesting to first look at the core losses and ensure they are similar for the two motors. There is a slight difference in slot shape, therefore tooth shape and area so we do not expect the plots to be identical - but to generally follow the same trends. This can be seen clearly in figure 6.8.

Next, it is important to see if the flux linkage is comparable for the two motors, and if this would contribute to any differences in the final efficiency maps. Figure 6.9 shows the q-axis flux contours (which is the only flux contributing to torque as explained in chapter 4) for both motors.

With the remaining losses compared the differences in figure 6.10 are attributed

to the stator copper losses. Note the differing shapes of the loss curves in figure 6.10. Figure 6.10 a) represents the stranded wound motor, and the trend which the contour plot follows is clear - the losses have a proportional relationship to output torque. In figure 6.10 b) we see a different trend. Losses appear to be more proportional to total power - they are changing with both torque and speed.

For both motors, curves appear to be smooth when plotted against current and slip, but are choppy in the torque speed profile. The efficiency and loss maps are calculated from previous two plots, but the smooth trend does not carry over. This is because the results in the torque speed profile are affected by the discontinuous optimization algorithm - which selects the optimal operating conditions for each point independent from the neighbouring points. It is also only applied to a finite number of points in the operating area.

Notice the very low speed range of the motor - even at high Torque the losses are very low for the bar wound motor. At these low speeds the effective resistance of the bar wound windings is very low despite a high applied current required to generate torque. With much lower resistance and therefore copper losses in the very low speed range, one can see that the low efficiencies seen for the strand wound motor a) are replaced by near peak efficiency values.

At high speeds we see the opposite phenomenon. Where the AC resistance is very high in the bar wound machine the efficiency drops well below what was seen in the stranded motor. The bar wound motor is outperformed by the stranded wound motor over most of its operating range.

Overall, the bar wound machine does not reach the same peak efficiency as the stranded wound machine - it is 89% efficient over most of its operating range rather

than 96%.

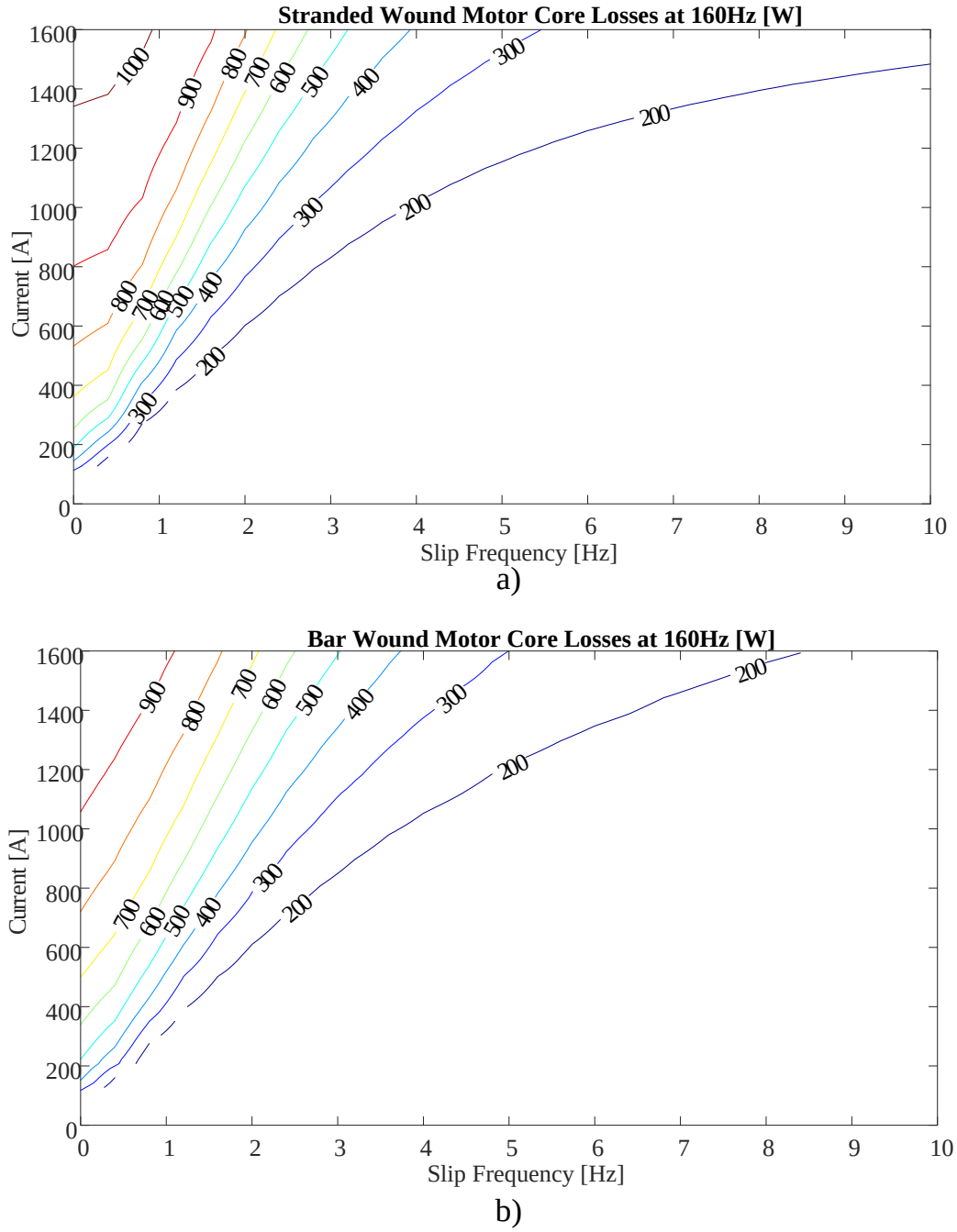

Figure 6.8: Core loss contour with current and slip at 160Hz for a) the stranded wound motor and b) the bar wound motor

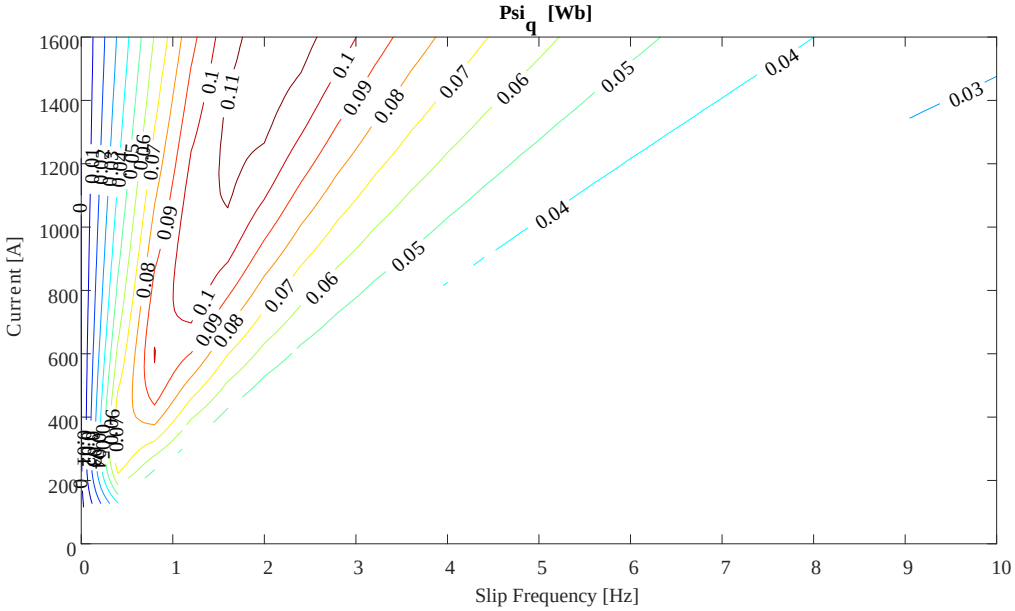

a)

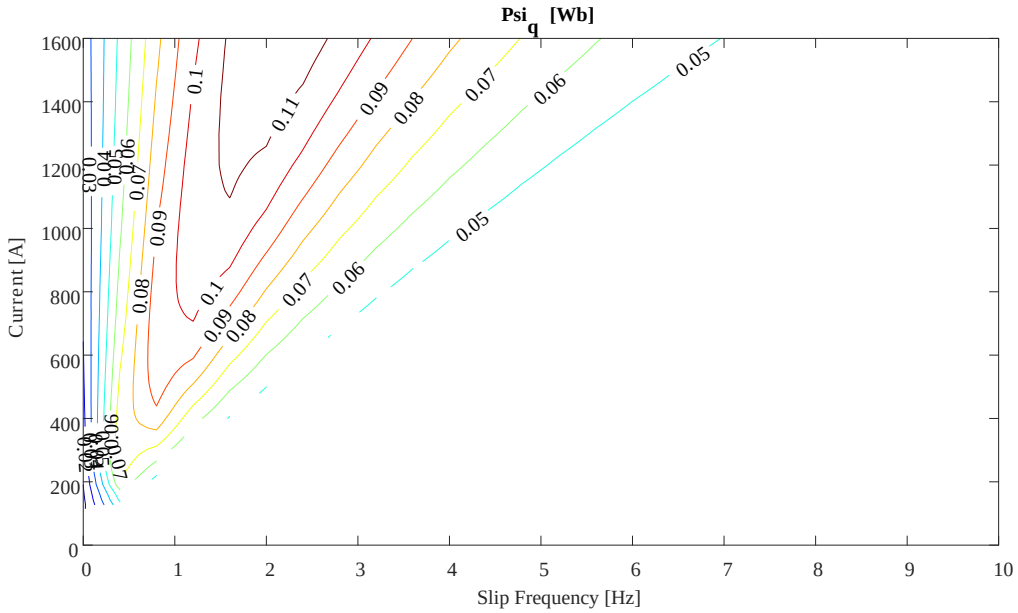

b)

Figure 6.9: Flux contour with current and slip at 160Hz for a) the stranded wound motor and b) the bar wound motor

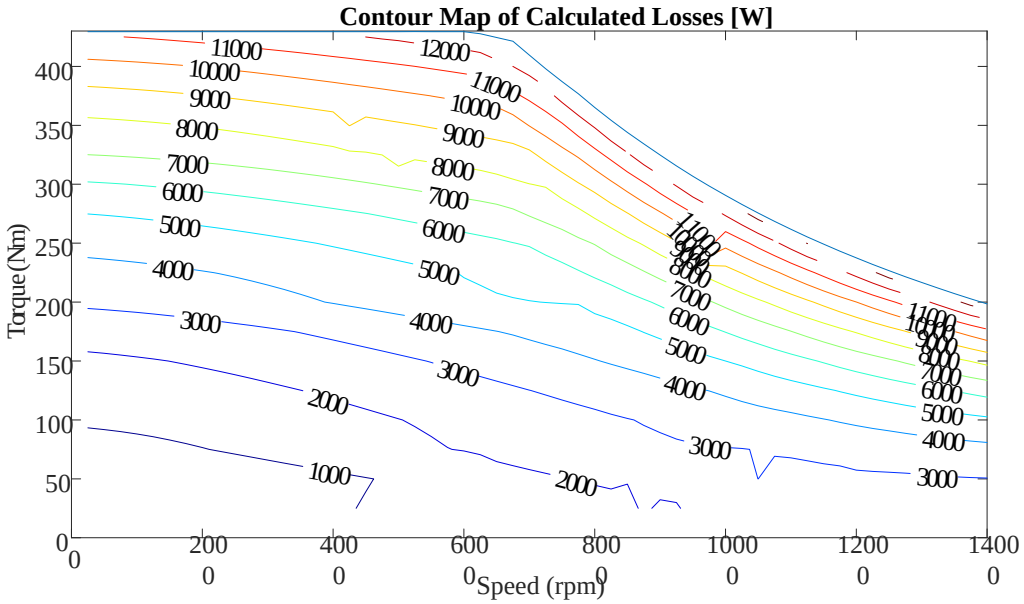

Figure 6.10: Side by side view of the calculated loss contour plots for a) the representative stranded wound machine and b) the bar wound machine.

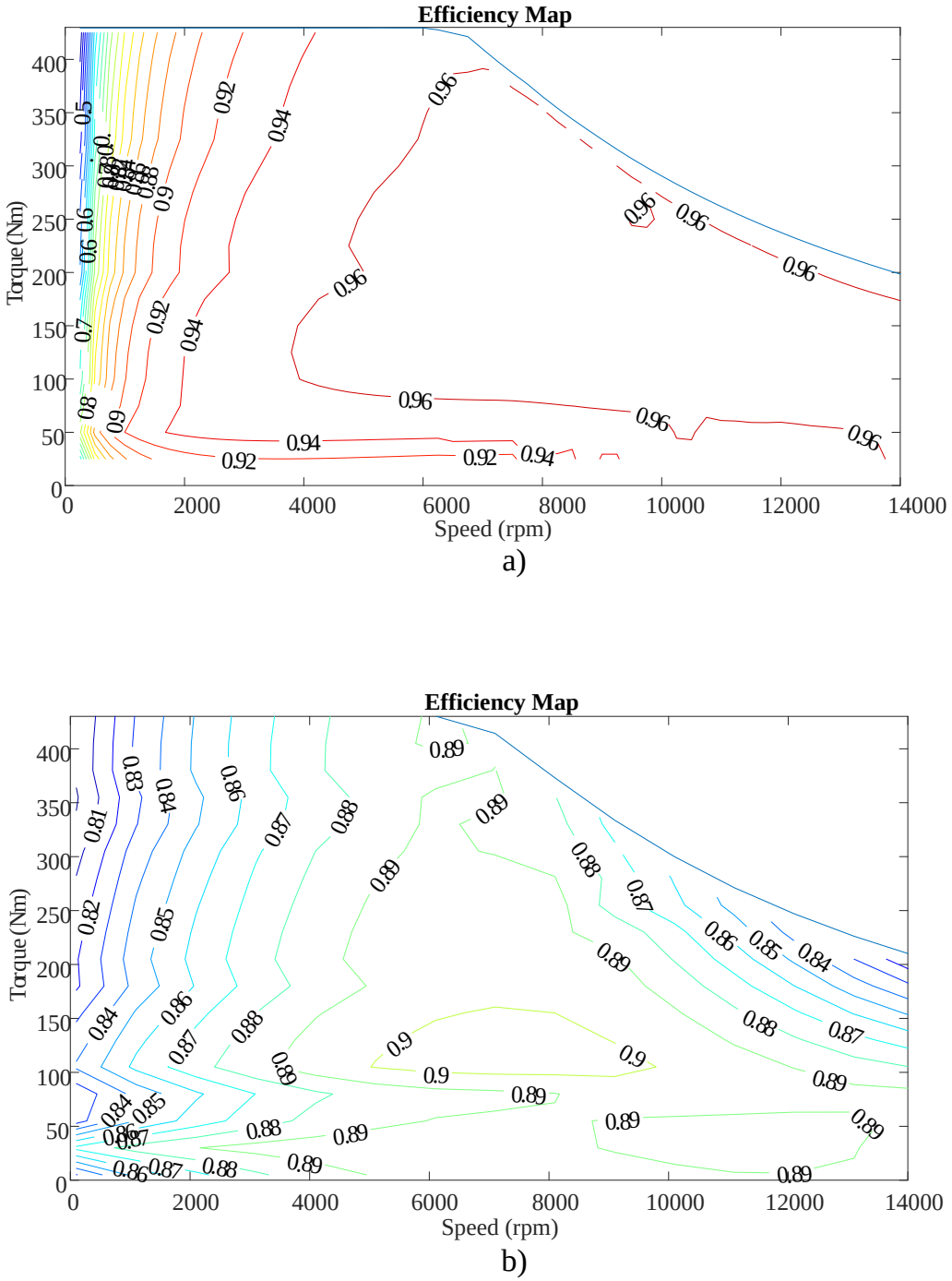

Figure 6.11: Side by side view of the efficiency maps for a) the representative stranded wound machine and b) the bar wound machine.

Chapter 7

Conclusions and Future Research

7.1 Summary and Review of Proposed Methodology

This thesis introduces a novel optimization based method of benchmarking an induction motor which has a number of distinct advantages:

1. The method compares only the optimal operating points for the motor. Induction motors are capable of reaching the user's desired torque and speed at a number of different current/slip combinations. This method minimizes the current required to reach the specified torque. This, by extension, minimizes the input power and maximizes the overall efficiency.

2. Only two sets of simulations are needed. One set of simulations at base speed is required where slip is swept from 0 to the break down slip and either input current or voltage is swept from 0 to the limiting current/voltage. The flux linkage and current must be measured in this set of simulations in addition

to the core losses and stator copper losses. The second set is much smaller and requires a small sweep of excitation frequencies, in this case 5, at nominal voltage and a slip of 0. In the absence of such a procedure, a large sweep of currents and slips would be needed at all excitation frequencies, and the results would be very difficult to organize into an efficiency map based on Torque and Speed. Literature review provided no method, to model the efficiency of an induction machine at a desired Torque and Speed.

3. The method automatically informs the user with some basic information about field-orientated control for maximum efficiency in the machine being modelled.

The proposed method of benchmarking an induction motor is first explained in Chapter 4 and is subsequently applied to an induction motor with stranded windings. For this motor, the model is able to correctly estimate the core losses within 4%. The algorithm is then applied to a motor of similar geometry with bar windings in chapter 6. No changes were made to the mathematics except for the addition of studying the stator copper losses, which was done with the same code used to study the core losses. This can easily be adapted to separately study eddy current losses in the core material, hysteresis losses, or whatever an engineer using the algorithm wishes to focus on minimizing. In this case the core losses were accurate within 4% and the stator copper losses were accurate within 5%.

The proposed algorithm is able to accurately model the losses and efficiencies of motors with different topologies and types of losses - with loss calculations always between 1% and 5% accuracy. A conservative estimate is made that the total simulation time using this method is about 1/28 or 3% of the total simulation time to create an efficiency map by an alternative methodology without mathematical optimization

and d-q axis analysis.

7.2 Summary of Comparative Analysis

The comparative analysis reveals that the stranded wound motor outperforms the bar wound machine over most of the operating range.

The torque speed curve generated with a current limit of $900\sqrt{2}$ A and a voltage limit equal to $u_{ds}^2 + u_{qs}^2 \leq (\frac{V_{dc}}{\sqrt{3}})^2$ is the same for both the bar wound and stranded wound motor. u_{ds} and u_{qs} depend on the current limit, speed, and flux leakage. It can be assumed then, since the same current limit is used, that the flux leakages are comparable. The flux contour plots were compared and found to be very similar. The same was done for core losses.

With the possibility that core losses or flux values differed greatly between the motors, any changes in the efficiency map can be attributed to differences in copper losses.

The efficiency maps differ greatly revealing that copper losses are only lower fo the bar wound motor at speeds lower than 1000-2000 rpm.

Based on the literature review, and the AC resistance of the GM motor, this speed range is much lower than anticipated. In figure 5.3 a comparison of AC resistance at a number of speeds vs. DC resistance was shown. For the 12 pole GM motor the AC resistance is lower until a speed of nearly 5000 rpm and this value can be expected to triple when the number of poles is divided by three.

In this case, the machine designed is not directly comparable to the GM motor and therefore the factor of three hypothesis does not hold. The GM machine has a much smaller slot opening, and 4-6 bars per slot. The machine has been optimized

and designed to include stator bars unlike the motor presented in this thesis.

The bar wound motor does offer a much higher peak torque when not limited by inverter current, and higher efficiency in the very low speed range. This is not practical for traction applications but may be desirable for an application where motors frequently run at low speeds. These areas of strength for the bar wound motor are without any optimization on winding layout or motor geometry to accommodate stator bars.

7.3 Opportunities for Additional Research

The benchmarking algorithm provided will allow for efficiency maps to be made with relatively little simulation data and computation time, which in turn should allow a researcher completing any suggested further research to quickly compare the efficiencies of motors being designed in order to reduce copper losses. The following are the major motor design areas suggested for optimization:

1. Slot shape including slot area and slot opening size
2. Position of stator bars within the slot, as distance from air gap has a large effect on eddy currents
3. Number and size of stator bars. Having a higher number of smaller stator bars set up in series (additional turns) or in parallel with insulation would mitigate eddy effects

If a motor is designed where the benchmarking process provided reveals an improved efficiency map - either with higher efficiency on the entire operating range or

in the range applicable to a certain application (such as the areas most used by a city driver at low speeds), the following topics should be investigated with simulations and experimental study:

1. Thermal performance
2. Noise and vibrations
3. Torque Ripple
4. Efficiency under various driving cycles

Refrences

[1] B. Bilgin, P. Magne, P. Malysz, Y. Yang, V. Pantelic, M. Preindl, A. Korobkine, W. Jiang, M. Lawford, and A. Emadi, "Making the Case for Electrified Transportation," *IEEE Transactions on Transportation Electrification*, vol. 1, no. 1, pp. 4–17, 2015.

[2] M. G. Waller, E. D. Williams, S. W. Matteson, and T. A. Trabold, "Current and theoretical maximum well-to-wheels exergy efficiency of options to power vehicles with natural gas," *Applied Energy*, vol. 127, pp. 55–63, 2014.

[3] James Weisheng Jiang, "Three-phase 24/16 switched reluctance machine for hybrid electric powertrains: design and optimization," p. 211, 2016.

[4] T. Finken, M. Felden, and K. Hameyer, "Comparison and design of different electrical machine types regarding their applicability in hybrid electrical vehicles," *Proceedings of the 2008 International Conference on Electrical Machines, ICEM'08*, pp. 1–5, 2008.

[5] A. Emadi, *Advanced Electric Drive Vehicles*, 2015.

[6] A. Veltman, D. Pulle, and R. De Doncker, *Fundamentals of Electrical Drives*. Dordrecht, Netherlands: Springer Netherlands, 2007.

[7] M. Stevens, "Electric Vehicle Sales in Canada: 2015 Final Numbers," 2016. [Online]. Available: http://www.fleetcarma.com/ev-sales-canada-2015/

[8] Tesla Motors, *MODEL S OWNER'S MANUAL*, 5th ed., 2013. [Online]. Available: https://www.tesla.com/sites/default/files/blog_attachments/model_s_owners_manual_europe_1

[9] M. Popescu and J. Goss, "Electric machine design for automotive applications," in *IEEE Energy Conversion Congress & Expo*, no. September, Milwaukee, WI, 2016, p. 64.

[10] Y. Tang, "Induction Motor Lamination Design," p. 14, 2012.

[11] Emerson Industrial, "Engineering Report: Form-Wound Coils Random-Wound Coils," North Mankato, MN, Tech. Rep., 2001.

[12] M. J. Islam, H. V. Khang, A. Repo, and A. Arkkio, "Eddy-Current Loss and Temperature Rise in the Form-Wound Stator Winding of an Inverter-Fed Cage Induction Motor," vol. 46, no. 8, pp. 3413–3416, 2010.

[13] S. Jurkovic, K. M. Rahman, and P. J. Savagian, "Design, optimization and development of electric machine for traction application in GM battery electric vehicle," *Proceedings - 2015 IEEE International Electric Machines and Drives Conference, IEMDC 2015*, pp. 1814–1819, 2016.

[14] F. Momen, K. Rahman, S. M. Ieee, Y. Son, and P. Savagian, "Electrical Propulsion System Design of Chevrolet Bolt Battery Electric Vehicle," 2016.

[15] K. M. Rahman, S. Jurkovic, C. Stancu, J. Morgante, and P. J. Savagian, "Design and Performance of Electrical Propulsion System of Extended Range Electric

Vehicle (EREV) Chevrolet Volt," *IEEE Transactions on Industry Applications*, vol. 51, no. 3, pp. 2479–2488, 2015.

[16] S. J. Chapman, "Electric Machinaery Fundamentals," *McGraw-Hill*, p. 746, 2003.

[17] D. G. Dorrell, A. M. Knight, M. Popescu, L. Evans, and D. A. Staton, "Comparison of Different Motor Design Drives for Hybrid Electric Vehicles," *2010 IEEE Energy Conversion Congress and Exposition*, pp. 3352–3359, 2010.

[18] J. D. Widmer, R. Martin, and M. Kimiabeigi, "Sustainable Materials and Technologies Electric vehicle traction motors without rare earth magnets," *SUSMAT*, vol. 3, pp. 7–13, 2015.

[19] Y. Tang, "Induction Motor With Improved Torque Density," 2010.

[20] ——, "AC Motor Winding Pattern," 2011.

[21] Y. Tang and S.-P. P. Luan, "Triple Layer Winding Pattern and Methods of Manufacturing Same," 2011.

[22] ——, "Dual Layer Winidng Pattern," 2012.

[23] D. Lyons, J. B. Straubel, E. Shahoian, and R. Garriga, "Rotor Design For An Electric Motor," Palo Alto, CA, 2013.

[24] S. G. Wirasingha, R. Gremban, A. Emadi, and S. Member, "Source-to-Wheel (STW) Analysis of Plug-in Hybrid Electric Vehicles," vol. 3, no. 1, pp. 316–331, 2012.

[25] H. C. Righolt and F. G. Rieck, "Energy chain and efficiency in urban traffic for ICE and," in *EVS27*, Barcelona, Spain, 2013, pp. 1–7.

[26] A. Emadi, S. Member, Y. J. Lee, S. Member, and K. Rajashekara, "Power Electronics and Motor Drives in Electric , Hybrid Electric , and Plug-In Hybrid Electric Vehicles," vol. 55, no. 6, pp. 2237–2245, 2008.

[27] V. T. Buyukdegirmenci, A. M. Bazzi, and P. T. Krein, "Evaluation of induction and permanent-magnet synchronous machines using drive-cycle energy and loss minimization in traction applications," *IEEE Transactions on Industry Applications*, vol. 50, no. 1, pp. 395–403, 2014.

[28] A. Emadi, *Energy-Efficient Electric Motors*, 3rd ed., Marlin Thurston, Ed. New York, New York: Marcel Drekker, 2005.

[29] B. Bilgin and A. Emadi, "Electric motors in electrified transportation: A step toward achieving a sustainable and highly efficient transportation system," *IEEE Power Electronics Magazine*, vol. 1, no. 2, pp. 10–17, 2014.

[30] P. Kumar, A. Dalal, and A. K. Singh, "Identification of Three Phase Induction Machines Equivalent Circuits Parameters Using Multi-Objective Genetic Algorithms," *2014 International Conference on Electrical Machines (ICEM)*, pp. 1211–1217, 2014.

[31] F. Endert, T. Heidrich, and A. Möckel, "Increased power density of permanent magnet synchronous machines by use of concentrated bar windings," *2012 2nd International Electric Drives Production Conference, EDPC 2012 - Proceedings*, pp. 1–5, 2012.

[32] X. Y. Ma, G. J. Li, G. Jewell, and Z. Q. Zhu, "Comparative study of short-pitched and fully-pitched SRMs supplied by sine wave currents," *Proceedings of*

the IEEE International Conference on Industrial Technology, vol. 2015-June, no. June, pp. 664–670, 2015.

[33] E. Engineering, A. V. Vidyapeetham, E. Engineering, A. V. Vidyapeetham, E. Engineering, and A. V. Vidyapeetham, "Induction Motor in short pitch and full," pp. 1–10, 2016.

[34] S. M. Lukic and A. Emadi, "MODELING OF ELECTRIC MACHINES FOR AUTOMOTIVE APPLICATIONS USING EFFICIENCY MAPS," in *Electrical Insulation Conference and Electrical Manufacturacting & Coil Winding Technology Conference*, Indianapolis, Indiana, 2003, pp. 543–550.

[35] S. S. Williamson, A. Emadi, and K. Rajashekara, "Comprehensive Efficiency Modeling of Electric Traction Motor Drives for Hybrid Electric Vehicle Propulsion Applications," vol. 56, no. 4, pp. 1561–1572, 2007.

[36] Y. Chen and Y. Perez, "Business Model Design : Lessons Learned from Tesla Motors," *Conference paper, Paris University*, no. August, 2015.

[37] M. N. Eisler, "A Tesla in every garage?" *IEEE Spectrum*, vol. 53, no. 2, pp. 34–55, 2016.

[38] K. Reynolds, "2013 Tesla Model S Reviews Car and Driver," 2015. [Online]. Available: http://www.caranddriver.com/reviews/2013-tesla-model-s-reviews

[39] A. Robinson, "2013 Tesla Model S P85+ Review - Long-Term Verdict," 2012. [Online]. Available: http://www.motortrend.com/cars/tesla/model-s/2013/2013-tesla-model-s-p85-review-verdict/

[40] P. K.-c. Kim, "Driving Characteristic Analysis of Traction Motors for Electric Vehicle by using FEM," 2014, pp. 0–5.

[41] R. T. Reid, "Motor Coil Winding Insertion Method and Apparatus," 2007.

[42] D. A. Gonzalez and D. M. Saban, "Study of the copper losses in a high-speed permanent-magnet machine with form-wound windings," *IEEE Transactions on Industrial Electronics*, vol. 61, no. 6, pp. 3038–3045, 2014.

[43] H. M. Hamalainen, J. J. Pyrhanen, and J. Puranen, "Minimizing skin effect in random wound high speed machine stator," *Ieee Eurocon 2009, Eurocon 2009*, no. 2, pp. 752–757, 2009.

[44] H. V. Khang and A. Arkkio, "Eddy-Current Loss Modeling for a Form-Wound Induction Motor Using Circuit Model," vol. 48, no. 2, pp. 1059–1062, 2012.